NASA Contractor Report 189143

# An Investigation of the Information Propagation and Entropy Transport Aspects of Stirling Machine Numerical Simulation

Louis F. Goldberg
*University of Minnesota*
*Minneapolis, Minnesota*

April 1992

Prepared for
Lewis Research Center
Under Service Contract Order C–22742–P

National Aeronautics and
Space Administration

C O N T E N T S

# N O T A T I O N

## ROMAN

### 1. Italicized Lower Case

| | |
|---|---|
| $g$ | scalar mass flux |
| $k$ | thermal conductivity |
| $l$ | length |
| $m$ | index limit |
| $n$ | index limit |
| $q$ | contact heat flux scalar |
| $r$ | radius |
| $s$ | condensation |
| $t$ | time |
| $v$ | velocity scalar |
| $x$ | displacement scalar |

### 2. Italicized Upper Case

| | |
|---|---|
| $A$ | area |
| $E$ | external and mutual energy |
| $K$ | constant |
| $M$ | mass |
| $N$ | non-dimensional parameter |
| $P$ | pressure |
| $Q$ | heat |
| $R$ | gas constant |
| $T$ | temperature |
| $U$ | internal energy |
| $V$ | volume |

### 3. Bold Italicized Lower Case

| | |
|---|---|
| $\mathbf{g}$ | mass flux density |

| | |
|---|---|
| $\boldsymbol{n}$ | unit outward normal |
| $\boldsymbol{q}$ | contact heat flux |
| $\boldsymbol{v}$ | velocity |
| $\boldsymbol{x}$ | displacement |

4. Bold Upper Case

| | |
|---|---|
| $\boldsymbol{T}$ | extra stress tensor |

5. Lower Case

| | |
|---|---|
| g | gravitational acceleration |
| p | particle |

GREEK

1. Upper Case

| | |
|---|---|
| $\Xi$ | entropy |
| $\Gamma$ | mole fraction |

2. Lower Case

| | |
|---|---|
| $\alpha$ | constant |
| $\kappa$ | thermal diffusivity |
| $\mu$ | dynamic viscosity |
| $\nu$ | kinematic viscosity |
| $\rho$ | density |
| $\psi$ | generalized scalar, vector, or tensor quantity |
| $\omega$ | angular velocity |

OPERATORS

| | |
|---|---|
| d | total derivative |

| | |
|---|---|
| D | substantive derivative |
| f() | function of |
| $\partial$ | partial derivative |
| $\Delta$ | incremental change |
| $\nabla$ | divergence |
| $\int$ | integral |
| $\Sigma$ | summation |
| $\bar{\psi} = {}_{[t]}\bar{\psi}$ | time average of $\psi$ |
| ${}_{[V]}\bar{\psi}$ | volume average of $\psi$ |
| ${}_{[tV]}\bar{\psi}$ | time average of volume average of $\psi$ |
| $\lvert\psi\rvert$ | absolute value or magnitude of $\psi$ |
| • | scalar product of vectors, vector product of vector and tensor |
| : | scalar product of tensors |

SUBSCRIPTS

| | |
|---|---|
| *a* | acoustic |
| *b* | boundary |
| *c* | cold cavity |
| *ch* | characteristic |
| *comp* | computational |
| *eff* | effective |
| *h* | hot cavity |
| *i* | index |
| *is* | isolated |
| *j* | index |
| *k* | index |
| *K* | Kurzweg |
| *Ma* | Mach |
| *(m)* | material body |
| *n* | momentum discrete volume |
| *Pr* | Prandtl |
| *Re* | Reynolds |
| *(s)* | system of particles |
| *sys* | system |
| *V* | at constant volume |
| *uw* | upwind |

| | |
|---|---|
| $Va$ | Valensi |
| 0 | fiduciary |
| $\Xi$ | at constant entropy |

SUPERSCRIPTS

| | |
|---|---|
| s | previous time step |
| * | distinguishing indicator |
| ^ | per unit mass |
| • | time rate of change |
| $j$ | index |

# INTRODUCTION

The activities described in this report cover two aspects pertinent to Stirling machine simulation, namely, information propagation and entropy transport. Information propagation issues have been shown in previous work to manifest themselves in hardware such as transmission lines (Go90). While such effects have not been definitely demonstrated for Stirling machines, there are enough suggestions (Go87, Go90) that such effects may be of concern in high frequency, high working pressure devices such as the Space Power Demonstrator Engine (SPDE) to warrant further study. Hence the work covered in this report is aimed essentially at attempting to determine whether the discretised primitive (or first order temporal differential) conservation balances are adequate to simulate information propagation effects in circumstances when they are known to be of importance.

Simulation of entropy in Stirling machines offers the opportunity of giving the designer new insights into the sources of irreversibilities as well as a criterion for judging the effectiveness of design optimizations. Previous oscillating flow work in this area has been effective in simulating the generation of entropy (Ko90) while less attention has been focussed on its transport through the computational domain. The work reported herein thus is aimed at correcting this imbalance by focussing on the transport of entropy which includes a means of constructing the computation domain as an isolated thermodynamic system.

Rather than simulating Stirling hardware directly, the approach adopted has been to base the simulation investigations on simple physical systems for which experimentally validated closed-form analytic solutions exist. Specifically, the information propagation study is based upon Iberall's analytic solution of the transmission line problem (Ib50) while the entropy transport investigation is carried out in terms of Kurzweg's oscillating flow apparatus (KZ84). This approach enables the behavior of the simulation in terms of information propagation and entropy transport to be studied in isolation. This avoids the complicating gas-dynamic interactions inherent in Stirling hardware from masking the effects under study and consequently leading to erroneous conclusions.

The report is divided into two parts. Part A describes the information propagation investigations while part B is devoted to the entropy transport work.

PART A

# INFORMATION PROPAGATION

## A.1 INTRODUCTION

The investigation of information propagation effects is carried out in terms of the following three tasks, namely:

*a.* The development of a new, non-pressure linked numerical algorithm for applying the mass, momentum and energy transport equations in one dimension and the application of the algorithm to Iberall's transmission line problem.

*b.* An investigation of the use of a hybrid explicit/implicit integration algorithm in Stirling machine simulation using the transmission line as a validation vehicle.

*c.* The development of an *n*-step (Go90) implicit temporal integration algorithm and its application to the transmission line to test whether the numerical integration algorithm itself influences the simulated information propagation behavior.

The analytic and physical details of Iberall's transmission line are described in detail in a previous NASA contractor report (no. 185285) (Go90) and hence will not be repeated here.

## A.2 ANALYTIC BACKGROUND

The essence of the pressure-linked algorithm is obtained by substituting the momentum equation into the continuity equation in which an equation of state is used to express density in terms of pressure. Following the derivation presented in Go90, the resulting equation may be expressed as:

$$\frac{{}_{[tV]}\bar{P}\,\bar{V}}{R\;{}_{[tV]}\bar{T}\,\Delta t} + \frac{\Delta t}{\bar{V}_{n(s)}}\int_{\bar{A}_{n(s)}}\left(\int_{\bar{A}_{(s)}} {}_{[tV]}\bar{P}\,\boldsymbol{n}\,d\bar{A}\right)\cdot\bar{-\boldsymbol{n}}\,d\bar{A}$$

$$= \frac{\bar{M}^{s}}{\Delta t} + \int_{\bar{A}_{n(s)}}\left(\left[\bar{\boldsymbol{g}}^{*} - {}_{[tV_n]}\bar{\rho}\,\bar{\boldsymbol{v}}_{n(s)}\right]\cdot\bar{-\boldsymbol{n}}\right)d\bar{A} \qquad \text{(A.2.1.1)}$$

where:

$$\bar{g}^{*} = \frac{({}_{[tV_n]}\bar{g}\bar{V}_{n(s)})^{s} + \Delta t\, f({}_{[tV_n]}\bar{g},\ {}_{[tV]}\bar{T},\ {}_{[tV]}\bar{\rho})}{\bar{V}_{n(s)}} \qquad (A.2.1.2)$$

This equation yields an advanced time or implicit pressure field. The information propagation characteristics of equation (A.2.1) may be demonstrated by applying it to a sequence of adjacent discrete volumes in a one-dimensional field of constant cross sectional area. Hence simplifying the equation and dropping the averaging notation for the sake of clarity yields:

$$P_{ii} + \sum_{j} \frac{\Delta t^2 A^2 RT}{V^2}(P_{ii} - P_{ij}) = K_{source} \qquad (A.2.2)$$

where $P_{ii}$ is the diagonal or "central" pressure term, $P_{ij}$ are the outlying pressures and $K_{source}$ is the source term. Now $V/A$ represents the length of the discrete volume in the computational direction and hence $V/A\Delta t$ represents a computational speed $v_{comp}$ since $\Delta t$ is the integration time increment. Thus equation (A.2.2) may be expressed as:

$$P_{ii}\left[1 + \sum_{j}\left(\frac{v_a}{v_{comp}}\right)_j^2\right] - \sum_{j}\left(\frac{v_a}{v_{comp}}\right)_j^2 P_{ij} = K_{source} \qquad (A.2.3)$$

where $v_a$ is the isothermal speed of sound for a fluid with constant specific heats. Thus, in simple terms, the information propagation is determined by the ratio $v_a/v_{comp}$ (acoustic speed to computational speed). This conveniently explains the behavior of the pressure linked analysis as it applies to the transmission line as well as, for that matter, to the SPDE (Go90, chapters 3 and 4). In particular, for the transmission line, it was observed that the transducer cavity to excitation pressure ratio asymptoted towards the value calculated via Iberall's analysis as the time step was decreased, which is a classic numerical result. Simultaneously, the phase angle between the excitation and transducer cavity started out at a value much higher than the Iberall prediction and decreased towards an asymptote with a value approximately half that predicted by Iberall as the integration time step was decreased. This phase angle behavior is explained by equation (A.2.3) since simply increasing $v_{comp}$ by decreasing $\Delta t$ decreases the coupling between $P_{ij}$ and $P_{ii}$ until the Courant limit defined by $v_a = v_{comp}$ is reached. Under these conditions, the phase angle predicted by equation (A.2.1) should correspond with the asymptotic value produced by a simulation in which the pressure field is extracted <u>explicitly</u> from the continuity equation, that is, without the use of any information propagation (or implicit pressure field) equation at all. Under these conditions, the requirement for using a unitary pressure domain (UPD) or equilibrium hypothesis for modelling information propagation (see Go90 section 2.6) would fall away and the criterion for determining the time step size is the achievement of numerical stability.

Noting that the information propagation modelling capability *per se* is quantified by the phase angle predictions, the above observations lead to the

proposition that the discretised primitive conservation balances intrinsically are deficient as a basis for simulating the information propagation effects occurring in a transmission line (specifically, low Mach number or stationary flow resonance induced shocks (Ji73)). Furthermore, by extension, this also may be true for the information propagation effects occurring in Stirling machines with characteristic numbers less than 24. These effects include the superposition of multiple reflected waves and microscopic scale regenerator choking.

The principal argument in support of the proposition arises from Iberall's analysis itself since Iberall does not solve the primitive conservation balances but in fact solves the Kirchoff equations of sound (Ib50, page 100, section 4). In particular, the relevant information propagation equation is obtained by substituting a simplified differential mass balance into a differential momentum balance which yields (quoting Rayleigh (St45), article 348, equation (2)):

$$\frac{dv}{dt} + \frac{1}{\rho_0}\frac{dP}{dx} = \frac{\mu}{\rho_0}\nabla^2 v + \frac{\mu}{3\rho_0}\frac{d^2 s}{dxdt} \qquad (A.2.4)$$

where $s$ is the "condensation" defined by:

$$s = \frac{\rho - \rho_0}{\rho_0} \qquad (A.2.5)$$

and $\rho_0$ is a constant, fiduciary density.

Equation (A.2.4) is the inverse symmetrical form of the well-known wave equation obtained by substituting the differential momentum balance into the differential mass balance. As noted by Organ (OJ89), a simplified isothermal form of the wave equation is given by:

$$\frac{1}{v_a^2}\frac{\partial^2 P}{\partial t^2} = \nabla^2 P \qquad (A.2.6)$$

which has the characteristics solution:

$$P = f(t \pm \frac{x}{v_a}) \qquad (A.2.7)$$

Hence in respect of accurately modelling information propagation effects, Iberall in effect agrees with Organ that the equations of sound should be used to extract the pressure field and not the primitive conservation balances. In the past, Organ has attempted to solve these equations using the method of characteristics (Or82), but, recognizing the intractability of this approach for the geometrical complexities of Stirling machines, he has resorted to a linear solution of equation (A.2.6) using the principle of superposition (OJ89). Implicit in this argument is the notion that the second order differential equation (A.2.6) is not equivalent (at least in numerically discretised terms) to the first order pressure-linked equation (A.2.1) even though their method of derivation is ostensibly the same (that is, substitution of a momentum equation into a continuity equation).

Rigorously, this can be shown to be the case since the integral transform of the complete version of equation (A.2.6) obtained via the generalized transport equation (Go90, equation (A.2.3)) is very different from equation (A.2.1). Therefore, this argument offers a reasonable explanation for the discrepancies observed to date between the predictions made by the simulation using equation (A.2.1) and Iberall's analysis - the simulation is based upon an effectively different description of information propagation.

However, if it is indeed true that the discretised primitive conservation balances used in the simulation inherently are incapable of describing the information propagation effects under discussion in this report, then all possible solutions of the primitive equations should show the same behavior, not just the pressure-linked forms evaluated to date. In particular, the symmetry between the second order differential Kirchoff momentum equation and the second order differential wave equation discussed above must also hold for the first order integral equations. Thus a solution obtained from the symmetrical form of the pressure-linked equation (A.2.1) not involving an implicit solution of the pressure field should show the same behavior as the pressure-linked form.

Therefore, if both symmetry and explicit solution bounding of an implicit solution can be demonstrated for the transmission line, then the proposition that the primitive discretised conservation balances are inadequate for modelling transmission line information propagation effects would gain significant substance.

A third element involved in this process is the notion that the qualitative information propagation modelling behavior of the primitive equations should be numerical integration process independent, particularly for the implicit forms. (It can be taken as read that this independence has been shown for explicit numerical integration, for example, see Roach (Ro82)). A means of testing this assertion is to implement the *n*-step implicit temporal integration scheme outlined in Go90 and apply it in both globally implicit and conventional (a matrix inversion at each time step) environments. In both cases, therefore, if the proposition is true, then the time step dependent phase angle behavior observed to date should be invariant.

The symmetry test is conducted in task *a*, the explicit solution bounding test forms task *b* while the implicit numerical invariancy test is carried out as task *c*.

## A.3 A NON-PRESSURE-LINKED INVERSE SYMMETRIC INTEGRAL FORMULATION

If the pressure-linked formulation of equation (A.2.1) is obtained by substituting the momentum conservation balance into the continuity equation, then the inverse symmetric form is obtained by substituting the continuity equation into the momentum conservation balance, so eliminating the pressures. Hence substituting the equation of state (Go90, equation (2.33)) into the continuity equation (Go90, equation (2.41)), temporally discretising the left hand side and rearranging produces:

$$ {}_{[tV]}\bar{P} \approx \frac{R\ {}_{[tV]}\bar{T}}{V}\left(\bar{M}^{s} + \frac{\Delta t}{\bar{V}}\int_{\bar{A}_{n(s)}} \{({}_{[tV_n]}\boldsymbol{g} - {}_{[tV_n]}\bar{\rho}\,\bar{\boldsymbol{v}}_{n(s)}) \cdot -\boldsymbol{n}\}d\bar{A}\right) \qquad (A.3.1) $$

Substituting equation (A.3.1) into the momentum equation (Go90, equation (2.42)) yields:

$$ \begin{aligned} \frac{d({}_{[tV_n]}\bar{\boldsymbol{g}}\,\bar{\boldsymbol{v}}_{n(s)})}{dt} &= \int_{\bar{A}_{(s)}} {}_{[tV]}\bar{\boldsymbol{g}}\{({}_{[tV]}\bar{\boldsymbol{v}} - \bar{\boldsymbol{v}}_{(s)}) \cdot -\boldsymbol{n}\}d\bar{A} - \bar{M}_{n(s)}\,\boldsymbol{g} \\ &- \int_{\bar{A}_{(s)}} \frac{R\ {}_{[tV]}\bar{T}\Delta t}{V}\left(\int_{\bar{A}_{n(s)}} ({}_{[tV_n]}\bar{\boldsymbol{g}} \cdot -\boldsymbol{n})\,d\bar{A}\right)\boldsymbol{n}\,d\bar{A} \\ &- \int_{\bar{A}_{(s)}} \frac{R\ {}_{[tV]}\bar{T}}{\bar{V}}\left[\bar{M}_{(s)} - \left(\int_{\bar{A}_{n(s)}} ({}_{[tV]}\bar{\rho}\,\bar{\boldsymbol{v}}_{n(s)} \cdot -\boldsymbol{n})\,d\bar{A}\right)\right]\boldsymbol{n}\,d\bar{A} \\ &- \int_{\bar{A}_{(s)}} \bar{\boldsymbol{g}}^{*}({}_{[V]}\bar{T}^{(t)},\ \nabla_{[tV]}\bar{\boldsymbol{v}},\ \nabla \cdot {}_{[tV]}\bar{\boldsymbol{v}})\,d\bar{A} \end{aligned} \qquad (A.3.2) $$

where $\bar{\boldsymbol{g}}^{*}$ represents the laminar and turbulent shear stress terms. Equation (A.3.2) yields the advanced time or implicit mass flux field $\boldsymbol{g}$. As before, the information propagation characteristics of the equation may be demonstrated by considering a sequence of adjacent discrete volumes in a one-dimensional field of constant cross-sectional area. Thus, temporally discretising the left hand side of equation (A.3.2), simplifying and dropping the averaging notation yields:

$$ \frac{g_{ii}V}{\Delta t} + A\sum_{j}\{(gv)_{ii} - (gv)_{ij}\} + \sum_{j}\frac{A^2RT\Delta t}{V}(g_{ii} - g_{ij}) = K_{source} \quad . $$

Rearranging, and noting that $v_{comp} = V/A\Delta t$ and $v_a^2 = RT$ yields:

$$ \begin{aligned} &(gv)_{ii}\left[\frac{v_{comp}}{v_{ii}} + \sum_{j}\left(1 + \frac{1}{N_{Ma}}\frac{v_a}{v_{comp}}\right)\right] - \sum_{j}\left(1 + \frac{1}{N_{Ma}}\frac{v_a}{v_{comp}}\right)(gv)_{ij} \\ &\quad = \frac{K_{source}}{A} \end{aligned} \qquad (A.3.3) $$

where $N_{Ma}$ is the Mach number. Therefore for the transmission line, the dominant term is $\frac{v_a}{v_{comp}N_{Ma}}$ since $N_{Ma} \ll 1$. This is also true in the Courant limit when $v_a = v_{comp}$. Hence the "information propagation" characteristics (in terms of mass flux) of equation (A.3.3) have a discretised description

different from those of the pressure-linked equation (A.2.1) and thus use of equation (A.3.2) provides a valid test for evaluating the symmetry of the primitive conservation balances.

Thus the set of steps comprising the solution algorithm becomes:

*a.* Guess the mass flux field $_{[tV_n]}\bar{g}^*$ .

*b.* Explicitly compute the discrete volume masses from Go90 equation (2.41) and then infer $_{[tV]}\bar{\rho}$ from known values of $\bar{V}_{(s)}$ .

*c.* Implicitly compute the temperature field using Go90 equation (2.43).

*d.* Explicitly compute the pressures from the equation of state (Go90 equation (2.33)).

*e.* Implicitly compute the mass flux field from equation (A.3.2).

*f.* Compare $_{[tV_n]}\bar{g}$ (computed) with $_{[tV_n]}\bar{g}^*$ (guessed) and return to step *b* with $f(_{[tV_n]}\bar{g}, {}_{[tV_n]}\bar{g}^*) \rightarrow {}_{[tV_n]}\bar{g}^*$ if the mass flux field is insufficiently converged.

## A.4 EXPLICIT SOLUTION BOUNDING FORM

The hybrid explicit/implicit algorithm proposed by MacCormack (Mc82) originally was investigated with a view to improving the efficiency of the existing purely implicit algorithm since it ostensibly offers a means of eliminating the iteration procedure on which the algorithm is based. MacCormack's algorithm may be viewed as a combination of two independent entities. The first is the hybrid explicit/implicit integration algorithm itself, while the second is an elaborate factorization procedure for extracting a pseudo-characteristics solution from the Navier-Stokes equations without explicitly solving an "information propagation" equation of the pressure-linked variety. However, the factorization procedure does not appear amenable to ready generalization (at least in discrete volume, integral terms) since it is derived for a conformal mesh (Cartesian in Mc82) using the partial differential form of the conservation equations.

In view of the discussion given in section A.2 above, only the hybrid explicit/implicit numerical algorithm portion of MacCormack's algorithm has been investigated since the pseudo-characteristics portion preempts an isolated evaluation of the primitive conservation balance inadequacy proposition. In other words, if MacCormack's full algorithm were to replicate Iberall's analytic results, it would not be possible to determine whether this was due to the implicit/explicit algorithm or the pseudo-characteristics

formulation. Thus in view of time and funding constraints, investigation of this latter aspect of MacCormack's algorithm as applied to a transmission line was not attempted.

The basic elements of MacCormack's hybrid explicit/implicit numerical integration algorithm (as applied to the integral conservation balances) may be described by the following sequence in terms of a general variable $\psi$:

*a*. Explicitly calculate the temporal gradient at the current time step:

$$\frac{d\psi}{dt}(t) = f(t,\psi(t)) \tag{A.4.1}$$

*b*. Implicitly extract an estimated advanced time value $\psi^*$ from:

$$\frac{d\psi^*}{dt}(t+\Delta t) = (1-\alpha)\frac{d\psi}{dt}(t) + \alpha f(t+\Delta t,\psi^*(t+\Delta t)) \tag{A.4.2}$$

*c*. Explicitly calculate the estimated advanced time temporal gradient:

$$\frac{d\psi^*}{dt}(t+\Delta t) = f(t+\Delta t,\psi^*(t+\Delta t)) \tag{A.4.3}$$

*d*. Implicitly extract a corrected advanced time value $\psi$ from:

$$\frac{d\psi}{dt}(t+\Delta t) = (1-\alpha)\frac{d\psi^*}{dt}(t+\Delta t) + \alpha f(t+\Delta t,\psi(t+\Delta t)) \tag{A.4.4}$$

*e*. Assemble an averaged final advanced time value:

$$\psi(t+\Delta t) = \psi(t) + \frac{1}{2}\Delta t\left[\frac{d\psi^*}{dt}(t+\Delta t) + \frac{d\psi}{dt}(t+\Delta t)\right] \tag{A.4.5}$$

In steps *b* and *c*, $\alpha$ is referred to as an "implicit blending factor".

On closer examination, the algorithm can be seen to be an interesting assembly of several existing methods. When $\alpha = .5$ (the numerical stability limit), steps *a* and *b* comprise a single iteration of the Crank-Nicholson algorithm while steps *c* and *d* comprise a single iteration of the standard implicit algorithm (in this case, $\alpha$ corresponds to the convergence factor). Step *e* represents an aggregation procedure similar to that found in the Runge-Kutta algorithm and its derivatives (such as those developed by Fehlberg and Verner).

The algorithm was applied to the standard set of pressure-linked integral equations and applied to the transmission line using the same parameters listed in Go90, section 4.9. In the first instance, the convergence of the algorithm at relatively large time steps (such as those generated by the UPD hypothesis) was quite poor (that is, large truncation errors). Hence several iterations of steps *c*, *d* and *e* were necessary in order to produce a stable solution. These iterations submerged the benefit of steps

*a* and *b*, in effect making them redundant. Furthermore, there was no change in the observed phase angle or amplitude ratio behavior in comparison with that shown by the standard Crank-Nicholson algorithm (Go90, sections 4.8 and 4.9).

Hence, in isolation, the particular explicit/implicit formulation of MacCormack does not contribute towards an understanding of the information propagation issues under discussion, in particular, it does not change the influence of the pressure-linked equation (A.2.1). Furthermore, it does not appear to yield any computational advantage in comparison with the standard iterative implicit method. However, it must be emphasized that these observations may not be true for MacCormack's method as a whole, that is, including the pseudo-characteristics formulation of the conservation equations.

Therefore, in order to ascertain the limiting behavior of the primitive conservation balances without the use of a pressure-linked formulation (as discussed in section 2), the standard implicit algorithm (Go90, section 2.5) is modified to remove the pressure-linked equation (A.2.1) so that the pressure field is extracted via an equation of state from the explicit mass conservation balance. The modified algorithm may be listed as follows:

*a*. Guess the mass flux field $_{[tV_n]}\overline{g}^*$ .

*b*. Explicitly compute the discrete volume masses from Go90 equation (2.41) and then infer $_{[tV]}\overline{\rho}$ from known values of $\overline{V}_{(s)}$ .

*c*. Explicitly compute the pressures from the equation of state (Go90 equation (2.33)) using current estimates of the advanced time temperature field.

*d*. Implicitly compute the temperature field using Go90 equation (2.43).

*e*. Implicitly compute the mass flux field from (Go90) equation (2.42) using the explicitly derived pressures of step *c* as part of the source term.

*f*. Compare $_{[tV_n]}\overline{g}$ (computed) with $_{[tV_n]}\overline{g}^*$ (guessed) and return to step *b* with $f(_{[tV_n]}\overline{g}, _{[tV_n]}\overline{g}^*) \rightarrow _{[tV_n]}\overline{g}^*$ if the mass flux field is insufficiently converged.

This algorithm allows the explicit information propagation boundary of the implicitly solved primitive conservation balances to be determined without introducing any complicating numerical effects.

## A.5 *n* - STEP IMPLICIT TEMPORAL INTEGRATION ALGORITHM

The *n* - step implicit algorithm is based upon a simple multi-increment expansion of the left hand side of the integral conservation balances. Consider a generalized form for the transport property $\psi$:

$$\frac{d_{[tV]}\overline{\psi}V}{dt} = f(t, {}_{[tV]}\overline{\psi}) \tag{A.5.1}$$

Discretising the left hand side linearly in terms of *n* time steps yields:

$$\frac{({}_{[tV]}\overline{\psi}V)^{j} - ({}_{[tV]}\overline{\psi}V)^{j-1}}{\Delta t/n} = f\left[t + \frac{j\Delta t}{n}, {}_{[tV]}\overline{\psi}^{j}\right] \tag{A.5.2}$$

where *j* is the time step index. Clearly, a linear expansion is not a necessary restriction, other expansions using, for example, sinusoidal or polynomial forms are equally valid. However, use of more complicated expansions does not affect the argument in principle, although such higher-order expansions probably yield superior numerical results.

Hence, in one-dimensional terms, if there are *m* discrete volumes, the solution is obtained from a system of $m \times n$ equations, each with the implicit form (after dropping the averaging notation for clarity):

$$-(K\psi)_{i}^{j-1} - (K\psi)_{i-1}^{j} + (K\psi)_{i}^{j} - (K\psi)_{i+1}^{j} = (K_{i}^{j})_{source} \tag{A.5.3}$$

where *i* is the spatial discretisation index. For the first time increment ($j = 1$), equation (A.5.3) becomes:

$$-(K\psi)_{i-1}^{j} + (K\psi)_{i}^{j} - (K\psi)_{i+1}^{j} = (K_{i}^{j})_{source} + \frac{(\psi V)^{s}}{\Delta t/n} \tag{A.5.4}$$

where the superscript s denotes the initial conditions.

In general, there is no restriction on $\Delta t$, *m* or *n* so that $\Delta t$ may be equated with the cycle period. Under these conditions, the algorithm becomes analogous to Gedeon's "globally implicit" technique with the important exception of equation (A.5.4), that is, the assumption that $\psi_{i}^{n} = \psi_{i}^{s}$ is <u>not</u> made. This version of the globally implicit technique yields a transient evolution of the flow field without imposing external cyclic closure boundary conditions. Furthermore, the *n* - step formulation is independent of the specific form of equation (A.5.1). Hence it can be applied to the pressure-linked equation (A.2.1), the symmetric momentum linked equation (A.3.2) as well as to the unmodified momentum and energy conservation balances (Go90, equations (2.42) and (2.43) respectively). Thus the iterative integration algorithms described in sections A.3 and A.4 and in Go90 section 2.5 may be used without alteration using the *n* - step formulation. This allows the integration algorithm independence of the primitive equations to be assessed

without adulteration by extraneous effects as required by the discussion in section A.2.

## A.6 RESULTS

The simulations are tested for two transmission line geometries and their respective boundary and excitation conditions as detailed in table A.1 giving a total of five test cases. The geometries and boundary conditions are identical to two of the test cases reported by Watts (Wa65). Particular care was taken to use exactly the same excitation pressure amplitudes as used experimentally. Where possible, the excitation frequencies were chosen to correspond with experimental tests in order to provide an experimental baseline for the comparison of the simulation and experimental data. In this regard, it must be pointed out that neither Watts nor Goldschmeid (Go68) report any experimental data for validating the phase angle predictions of equation (116) in Ib50. Hence it is assumed here that because Iberall's amplitude ratio predictions (also obtained from equation (116)) are confirmed by experiment, his phase angle predictions are likewise valid. However, this may not be true, a qualification which must be borne in mind when reviewing the results presented below.

The six inch line excited at 100 Hz has a characteristic number[1] ($N_{ch}$) of 22.86 (see table A.2) and is equivalent in information propagation terms to the SPRE which has $N_{ch} = 24$. Hence to the extent that the information propagation effects occurring in the transmission line match those occurring in the SPRE (as alluded to in section A.2, this similarity may be only nominal), the simulation comparisons provide a test of the information propagation modelling validity of the simulations as applied to the SPRE.

The results for the five test cases are given in tables A.2 through A.6 located at the end of this section and are presented in terms of amplitude ratio and phase angle. The amplitude ratio is defined as the ratio between the transducer cavity and excitation pressure amplitudes while the phase angle is the phase lag between the excitation and transducer cavity waveforms. With reference to tables A.2 through A.6, the first line reports the analytic predictions of Iberall's analysis and the second line gives the amplitude ratio measured by Watts (Wa65) (where available). Thereafter, the tabulation gives the results of eight different simulations each corresponding to a different integration algorithm / equation formulation mix.

The first and third simulations correspond to the UPD and equilibrium information propagation hypotheses (defined in Go90, section 2.6) using the pressure-linked equation (A.2.1) (obtained by solving the continuity equation after substitution of the momentum equation, hence the "UPD: continuity" and "Equilibrium: continuity" nomenclature).

---

[1]The characteristic number $N_{ch}$ is defined as the number of pressure wave traverses occurring per cycle over the entire extent of the working space.

Table A.1 Transmission line geometries

| Parameter | 6 inch line | 24 inch line |
|---|---|---|
| Length (mm) | 152.4 | 609.6 |
| Diameter (mm) | 4.66 | 4.66 |
| Cavity volume ($cm^3$) | .414 | .414 |
| Gas type | air | air |
| Mean pressure (bar) | .77 | .77 |
| Excitation pressure amplitude (bar) | .00077 | .00077 |
| Temperature (°C) | 28.9814 | 25.95 |
| Excitation frequencies (Hz) | 100; 230; 400 | 55; 110 |

The second and fourth simulations portray the UPD and equilibrium information propagation hypotheses using the symmetric momentum equation (A.3.2) (obtained by solving the momentum equation after substitution of the continuity equation yielding the "UPD: momentum" and "Equilibrium: momentum" nomenclature). Both equilibrium simulations are performed at 50 and 100 increments per cycle in order to confirm the phase angle and amplitude ratio behavior. The first four simulations are thus designed to accomplish the symmetry test.

The fifth simulation uses the algorithm described in section A.4 (explicit solution bounding) in which the momentum and energy balances are solved implicitly and the pressure field is determined explicitly without a pressure-linked equation. The number of increments per cycle is chosen purely on the basis of numerical stability, being small enough to achieve a stable solution but not so small as to undercut the Courant criterion and introduce dispersion errors (Ro82).

The last three simulations test various forms of the *n* - step implicit algorithm. The sixth simulation is based on the UPD hypothesis for determining the number of time steps per cycle, while each time step is divided into *n* substeps. Four values of *n* are tested in order to establish the behavioral trends of the amplitude ratio and phase angle. The seventh simulation embodies the globally implicit version of the *n* - step implicit algorithm while the last simulation is similar to the "UPD: *n* - step implicit" simulation except that the time steps are variable and are determined characteristically at each stage of the simulation.

The results for the test case approximating the SPRE in transmission line information propagation terms are given in table A.2 (6 inch length with 100 Hz excitation). This case yields an analytic characteristic number of 22.862 which is confirmed within a tolerance of $\pm$.002 by all the simulations.

Iberall's analysis predicts an amplitude ratio close to unity and .03 higher than that measured (the measured value is read manually off a logarithmic graph in Wa65 and therefore is only approximate) while the predicted phase angle of .5° is small. The predictions made by the momentum and continuity linked equations are identical and show the same trends as the time step size is decreased (number of increments per cycle is increased). As noted before, these trends are typified by the amplitude ratio increasing towards the Iberall value as the time step size is decreased while, concomitantly, the phase angle decreases. Hence, in this case, the symmetry of the equations is demonstrated.

The simulation with no pressure linking using 300 increments per cycle produces an amplitude ratio equal to that produced by the 100 increment per cycle equilibrium algorithm (at least to three decimal places) and a phase angle lower than that produced at 100 increments per cycle. Hence, in this case as well, an explicit determination of pressure indeed does produce a bounding value of amplitude ratio and phase angle for the implicit continuity and momentum linked equation algorithms.

Without going into needless repetitive detail, these observations apply for the remaining test cases as well (tables A.3 through A.6). A few interesting points to note are:

- In table A.4, at 400 Hz excitation, Iberall's analysis underpredicts the experimental amplitude ratio by 31% while the asymptotic simulated pressure amplitude ratio for the first five simulations of 3.301 is 15% less than Iberall's value and 41% less than that measured.

- Also in table A.4, the equilibrium simulations as well as the case with no pressure linking show identical results at a temporal discretisation of 100 increments per cycle. This further demonstrates that the explicit pressure determination defines the bounding case of the implicit determination using either continuity or momentum equation linking.

- In table A.6, a comparison of the predictions of the equilibrium simulations with the predictions produced by the simulation with no pressure linking shows that when the temporal discretisation of the explicit pressure simulation is coarser than that of the implicit simulations, then the implicit simulations predict phase angles smaller and amplitude ratios larger than the explicit simulation. This conforms to the standard time step size dependent trend and shows that at small enough time steps, extracting the pressure field implicitly via the continuity and momentum linked equations is computationally redundant.

Therefore, the first five simulations demonstrate that the continuity and momentum equation linked equations are indeed symmetric and that the implicitly extracted pressure fields are the same as those extracted explicitly at small enough time steps. In other words, explicit pressure bounding for the primitive conservation balances is confirmed.

Consequently, the remaining $n$ - step implicit simulations were carried out using the momentum linked formulation as it is numerically more efficient than its symmetrical continuity or pressure-linked counterpart because one less matrix inversion is required for each iteration.

Reverting to table A.2, it may be observed that the UPD and characteristically determined time step versions (numbers 6 and 8) produce identical results in terms of amplitude ratio versus increments per time step. The trend in both cases conforms to the standard pattern, namely, amplitude ratio increasing with decreasing sub-time step size. Furthermore, the amplitude ratio at 13 increments per time steps conforms to the limiting value produced by the single step implicit simulations (numbers 3 and 4). In terms of phase angle behavior, the UPD and characteristic versions of the $n$ - step implicit algorithm show the same trend (phase angle decreasing with increasing number of increments) except that there is some disparity between the numerical values. This is caused by the relative lack of cyclic convergence of the characteristic version (cyclic energy balance errors > 1% versus equivalent errors for the UPD version < .01%). The characteristic version takes an inordinately large number of cycles to reach cyclic equilibrium and hence the simulation was terminated before full convergence was achieved as a matter of expediency. Hence the characteristic version, while being a useful test of numerical algorithm independence, is not a practical methodology.

Finally, the behavior of the $n$ - step globally implicit algorithm shown in table A.2 is rather interesting. A discretisation of 20 increments per cycle proved to be the largest practical value that would enable the coefficient matrices to be inverted (using a computer with a 64 bit precision word length) before numerical round-off errors caused the simulation to become unstable. This situation could be alleviated somewhat by various normalization schemes as well as by matrix partitioning algorithms. However, in the context of this investigation, such endeavors would not add materially to the outcome and hence were not attempted. In this context, the $n$ - step globally implicit scheme conforms to the established pattern of amplitude ratio and phase angle behavior observed for all the other simulations. Examining the phase angle behavior, one is tempted to infer that the value asymptotes to the Iberall value of .525°. However, in temporal discretisation terms, at 20 increments per cycle, the algorithm is in the range of the UPD algorithm, which with $N_{Ch} = 22.864$ yields a temporal discretisation of 23 increments per cycle. Thus at 20 increments per cycle, the $n$ - step globally implicit algorithm produces a phase angle greater than the 23 increment per cycle UPD algorithm which is in conformity with the established trend.

With minor variations, these observations also apply to the results produced by the $n$ - step implicit simulations for all the remaining test cases in tables A.3 through A.6. The only exceptions worth noting occur in tables A.4 and A.6 in which the phase angle produced by the globally implicit simulation at 10 increments per cycle is greater than that produced at 5 increments per cycle. Once again, these exceptions are caused by cyclic equilibrium convergence effects where the particular simulations are not as converged as their counterparts. However, since the phase angles in all cases at 20 increments per cycle are less than those at coarser discretisations, the basic behavioral trend is not violated.

Therefore, the *n* - step globally implicit simulations confirm that the simulation predictions are independent of the particular form of the integration algorithm used to solve the conservation balances. Furthermore, use of an *n* - step implicit algorithm does not appear to offer any numerical accuracy advantages that cannot be achieved at a lower computational cost using a single step implicit Crank-Nicholson algorithm with a finer temporal discretisation. In this vein, there does not appear to be any advantage in using a globally implicit algorithm, at least in terms of a strict transient simulation.

Table A.2 6 inch transmission line with 100 Hz excitation

| Reference Number | Analysis | Temporal Discretisation Parameter | Parameter Value | Char. Number | Amplitude Ratio | Phase Angle (deg) |
|---|---|---|---|---|---|---|
| -- | Iberall (analytic) | -- | -- | 22.862 | 1.060 | 0.525 |
| -- | Watts (exper.) | -- | -- | -- | 1.03 | -- |
| 1 | UPD: continuity | -- | -- | 22.864 | 1.049 | 0.97 |
| 2 | UPD: momentum | -- | -- | 22.864 | 1.049 | 0.97 |
| 3 | Equilibrium: continuity | Increments per cycle | 50 | 22.864 | 1.051 | 0.59 |
| | | | 100 | 22.864 | 1.052 | 0.41 |
| 4 | Equilibrium: momentum | Increments per cycle | 50 | 22.864 | 1.051 | 0.59 |
| | | | 100 | 22.864 | 1.052 | 0.41 |
| 5 | Implicit: no pressure linking | Increments per cycle | 300 | 22.864 | 1.052 | 0.32 |
| 6 | UPD: *n* - step implicit | Increments per time step | 2 | 22.864 | 1.050 | 0.80 |
| | | | 3 | 22.864 | 1.051 | 0.56 |
| | | | 5 | 22.864 | 1.052 | 0.38 |
| | | | 13 | 22.864 | 1.052 | 0.31 |
| 7 | *n* - step globally implicit | Increments per cycle | 5 | 22.864 | 1.011 | 2.69 |
| | | | 10 | 22.864 | 1.038 | 1.98 |
| | | | 20 | 22.864 | 1.048 | 1.11 |
| 8 | *n* - step implicit: character- istically determined time step | Increments per time step | 2 | 22.860 | 1.050 | 0.54 |
| | | | 3 | 22.860 | 1.051 | 0.54 |
| | | | 5 | 22.860 | 1.052 | 0.43 |
| | | | 13 | 22.860 | 1.052 | 0.18 |

Table A.3 6 inch transmission line with 230 Hz excitation

| Reference Number | Analysis | Temporal Discretisation Parameter | Parameter Value | Char. Number | Amplitude Ratio | Phase Angle (deg) |
|---|---|---|---|---|---|---|
| -- | Iberall (analytic) | -- | -- | 9.940 | 1.381 | 2.095 |
| -- | Watts (exper.) | -- | -- | -- | -- | -- |
| 1 | UPD: continuity | -- | -- | 9.942 | 1.232 | 10.52 |
| 2 | UPD: momentum | -- | -- | 9.942 | 1.232 | 10.52 |
| 3 | Equilibrium: continuity | Increments per cycle | 50 | 9.942 | 1.332 | 2.81 |
| | | | 100 | 9.943 | 1.336 | 1.68 |
| 4 | Equilibrium: momentum | Increments per cycle | 50 | 9.942 | 1.332 | 2.81 |
| | | | 100 | 9.943 | 1.336 | 1.67 |
| 5 | Implicit: no pressure linking | Increments per cycle | 200 | 9.943 | 1.338 | 1.10 |
| 6 | UPD: *n* - step implicit | Increments per time step | 2 | 9.942 | 1.302 | 6.06 |
| | | | 3 | 9.942 | 1.318 | 3.78 |
| | | | 5 | 9.942 | 1.329 | 2.86 |
| | | | 10 | 9.942 | 1.335 | 1.72 |
| 7 | *n* - step globally implicit | Increments per cycle | 5 | 9.942 | 1.052 | 13.73 |
| | | | 10 | 9.942 | 1.228 | 10.66 |
| | | | 20 | 9.942 | 1.304 | 6.15 |
| 8 | *n* - step implicit: characteristically determined time step | Increments per time step | 2 | 9.938 | 1.301 | 6.18 |
| | | | 3 | 9.938 | 1.318 | 3.74 |
| | | | 5 | 9.938 | 1.329 | 2.85 |
| | | | 10 | 9.938 | 1.335 | 1.69 |

Table A.4 6 inch transmission line with 400 Hz excitation

| Reference Number | Analysis | Temporal Discretisation Parameter | Parameter Value | Char. Number | Amplitude Ratio | Phase Angle (deg) |
|---|---|---|---|---|---|---|
| -- | Iberall (analytic) | -- | -- | 5.716 | 3.885 | 10.886 |
| -- | Watts (exper.) | -- | -- | -- | 5.6 | -- |
| 1 | UPD: continuity | -- | -- | 5.718 | 1.208 | 40.12 |
| 2 | UPD: momentum | -- | -- | 5.718 | 1.209 | 40.18 |
| 3 | Equilibrium: continuity | Increments per cycle | 50 | 5.721 | 3.180 | 15.86 |
| | | | 100 | 5.721 | 3.301 | 9.04 |
| 4 | Equilibrium: momentum | Increments per cycle | 50 | 5.720 | 3.180 | 15.85 |
| | | | 100 | 5.721 | 3.301 | 9.03 |
| 5 | Implicit: no pressure linking | Increments per cycle | 100 | 5.721 | 3.301 | 9.07 |
| 6 | UPD: *n* - step implicit | Increments per time step | 2 | 5.719 | 1.997 | 39.21 |
| | | | 3 | 5.720 | 2.470 | 32.55 |
| | | | 9 | 5.721 | 3.171 | 14.76 |
| | | | 17 | 5.721 | 3.285 | 8.96 |
| 7 | *n* - step globally implicit | Increments per cycle | 5 | 5.717 | 1.029 | 38.78 |
| | | | 10 | 5.718 | 1.791 | 42.70 |
| | | | 20 | 5.720 | 2.604 | 31.52 |
| 8 | *n* - step implicit: character- istically determined time step | Increments per time step | 2 | 5.712 | 1.972 | 38.84 |
| | | | 3 | 5.712 | 2.412 | 34.08 |
| | | | 9 | 5.711 | 3.123 | 19.48 |
| | | | 17 | 5.711 | 3.281 | 14.80 |

Table A.5 24 inch transmission line with 55 Hz excitation

| Reference Number | Analysis | Temporal Discretisation Parameter | Parameter Value | Char. Number | Amplitude Ratio | Phase Angle (deg) |
|---|---|---|---|---|---|---|
| -- | Iberall (analytic) | -- | -- | 10.340 | 1.299 | 3.607 |
| -- | Watts (exper.) | -- | -- | -- | -- | -- |
| 1 | UPD: continuity | -- | -- | 10.341 | 1.162 | 8.62 |
| 2 | UPD: momentum | -- | -- | 10.341 | 1.162 | 8.62 |
| 3 | Equilibrium: continuity | Increments per cycle | 50 | 10.341 | 1.234 | 3.22 |
| | | | 100 | 10.341 | 1.237 | 2.50 |
| 4 | Equilibrium: momentum | Increments per cycle | 50 | 10.341 | 1.234 | 3.23 |
| | | | 100 | 10.341 | 1.237 | 2.50 |
| 5 | Implicit: no pressure linking | Increments per cycle | 170 | 10.341 | 1.238 | 2.23 |
| 6 | UPD: *n* - step implicit | Increments per time step | 2 | 10.341 | 1.214 | 5.47 |
| | | | 3 | 10.341 | 1.226 | 4.03 |
| | | | 5 | 10.341 | 1.233 | 3.32 |
| | | | 10 | 10.341 | 1.237 | 2.53 |
| 7 | *n* - step globally implicit | Increments per cycle | 5 | 10.341 | 1.032 | 11.30 |
| | | | 10 | 10.341 | 1.161 | 8.68 |
| | | | 20 | 10.341 | 1.214 | 5.50 |
| 8 | *n* - step implicit: character- istically determined time step | Increments per time step | 2 | 10.338 | 1.215 | 5.16 |
| | | | 3 | 10.338 | 1.226 | 4.25 |
| | | | 5 | 10.338 | 1.234 | 3.50 |
| | | | 10 | 10.338 | 1.238 | 2.84 |

Table A.6 24 inch transmission line with 110 Hz excitation

| Reference Number | Analysis | Temporal Discretisation Parameter | Parameter Value | Char. Number | Amplitude Ratio | Phase Angle (deg) |
|---|---|---|---|---|---|---|
| -- | Iberall (analytic) | -- | -- | 5.170 | 4.252 | 25.419 |
| -- | Watts (exper.) | -- | -- | -- | 4.8 | -- |
| 1 | UPD: continuity | -- | -- | 5.171 | 1.008 | 40.10 |
| 2 | UPD: momentum | -- | -- | 5.171 | 1.008 | 40.11 |
| 3 | Equilibrium: continuity | Increments per cycle | 50 | 5.174 | 3.070 | 19.60 |
| | | | 100 | 5.174 | 3.209 | 13.26 |
| 4 | Equilibrium: momentum | Increments per cycle | 50 | 5.174 | 3.070 | 19.60 |
| | | | 100 | 5.174 | 3.209 | 13.26 |
| 5 | Implicit: no pressure linking | Increments per cycle | 90 | 5.174 | 3.196 | 13.99 |
| 6 | UPD: *n* - step implicit | Increments per time step | 2 | 5.172 | 1.743 | 43.62 |
| | | | 3 | 5.173 | 2.211 | 38.82 |
| | | | 10 | 5.174 | 3.063 | 19.55 |
| | | | 20 | 5.174 | 3.204 | 13.30 |
| 7 | *n* - step globally implicit | Increments per cycle | 5 | 5.171 | 1.007 | 39.91 |
| | | | 10 | 5.172 | 1.743 | 43.97 |
| | | | 20 | 5.173 | 2.512 | 33.88 |
| 8 | *n* - step implicit: characteristically determined time step | Increments per time step | 2 | 5.167 | 1.798 | 42.56 |
| | | | 3 | 5.167 | 2.262 | 37.81 |
| | | | 10 | 5.166 | 3.069 | 19.14 |
| | | | 20 | 5.166 | 2.942 | 16.79 |

## A.7 CONCLUSION

The results confirm that the discretised primitive integral conservation balances have the following features:

- they are mathematically symmetrical with respect to continuity and momentum equation linking.

- when they are solved implicitly, as the time increment is decreased, the pressure field solution obtained using either a continuity or momentum linked equation set approaches the solution obtained explicitly from the continuity equation via an equation of state.

- in terms of the transmission line, their solution is independent of the form of the implicit numerical integration algorithm used.

Therefore, in the light of these confirmations, it seems reasonable to conclude that the discretised pressure or mass flux linked primitive conservation balances used in the simulations are not unconditionally valid for modelling transmission line information propagation effects at characteristic numbers less than about 24. To the extent that these specific effects are also present in Stirling machines (in particular, the SPDE and SPRE), it is consistent to infer that Stirling machine simulations based on these primitive conservation balances are also open to question.

In particular, at low characteristic numbers, neither the pressure-linked nor mass-linked formulations appear to replicate the physical behavior described by the Kirchoff momentum equation or by the wave equation, despite attempts to impose a characteristics solution on the pressure-linked formulation using either a UPD or a characteristically determined, variable time step hypothesis.

This position is supported by Iberall's analysis itself, by the results of Organ's linear wave equation approach (OJ89) as well as by MacCormack's analysis (Mc82).

PART B

# ENTROPY TRANSPORT

## B.1 INTRODUCTION

The investigation of entropy transport resolved itself into two tasks. In the first task, a previously developed suite of codes used for simulating the Mechanical Engineering Test Rig (METR) (Go90) was applied to Kurzweg's apparatus and validated against his experimental and closed-form analytic data. Thereafter, an entropy transport equation was developed and evaluated in the validated codes. These activities may be resolved into the following specific tasks:

*a*. The adaptation of the Mechanical Engineering Test Rig (METR) one- and two-dimensional codes (Go90) to Kurzweg's enhanced diffusion oscillating flow test apparatus (KZ84).

*b*. The formulation of an entropy postulate and its rigorous transformation into an entropy transport equation to be tested in a code applied to Kurzweg's apparatus.

## B.2 INITIAL OBSERVATIONS

Kurzweg's apparatus is based on incompressible (water) fluid flow. However, in view of NASA's interest in the compressible oscillating flows occurring in Stirling cycle machines, it was originally intended to simulate Kurzweg's apparatus using a compressible fluid. This was also logistically prudent since the METR codes are strictly appropriate for compressible flows. However, early on during task *a* it became clear that the original intention of using a compressible fluid was not feasible for at least the following reasons:

- reference KZ84 provides insufficient geometrical detail about the variable volume cavities at either end of the capillary tube bundle to enable the compressible flow boundary conditions to be specified completely.

- in order to remain within the laminar flow regime specified for the applicability of the analysis described in KZ84, very small compressible flow oscillation frequencies and tidal displacements are required. Under these conditions, other effects not accounted for by Kurzweg (such as buoyancy effects) may be expected to influence the results. In this case, the validity of the experimental data in KZ84 under compressible flow conditions is questionable.

Thus it was decided to enhance the METR codes to describe incompressible flows also so that they could be applied directly to Kurweg's apparatus without the above two limitations.

Initial validation efforts with the two-dimensional code at the chosen test point (see section B.3), consistently yielded effective diffusivities four to five times larger than those measured or predicted analytically. The simulation was found to be very sensitive to axial discretisation so that each decrease in discrete volume axial length decreased the simulated effective diffusivity, edging it ever closer to the nominal experimental value. At a discretisation of 1 discrete volume per millimeter, the overprediction had been reduced to a factor of 2 at the expense of a very large increase in computational effort, almost overwhelming the computer equipment available for the project.

These observations are *prima facie* evidence of the ubiquitous "false diffusion" problem that plagues numerical analysis in general and integral analysis in particular. Hence further progress mandated the development of an algorithm for eliminating the false diffusion problem inherent in the discretised integral description of the continuum mechanics used in the simulation. This made inclusion of entropy transport in the simulations of vital importance, since false diffusion correction schemes do have the potential for violating the second law of thermodynamics.

In order to develop such a false diffusion correction algorithm, it was judged prudent to do the development work using a one-dimensional simulation of Kurzweg's apparatus rather than a two-dimensional code since this was felt to be more time-effective in the long run. Furthermore, since the one-dimensional simulation uses the standard Kays and London (KL64) steady-state heat transfer coefficient and friction factor correlations, such a simulation provides another experimentally based test point for evaluating the accuracy of such correlations in describing oscillating flows.

## B.3 TEST CONDITIONS

The test apparatus simulated is shown in figure B.1. Essentially, the device consists of an upper and a lower cavity joined by an acrylic tube containing a bundle of glass tubes. These tubes apparently are not fitted into a manifold at either end so that the net flow area consists of the internal tube areas as well as the triangular areas between the tubes (figure B.2). The external axial faces of the hot and cold reservoirs are fitted with flexible membranes so that when the entire apparatus is oscillated by a shaker, the fluid (water) will undergo corresponding oscillations. Finally, the apparatus is cocooned in insulation so maintaining a nominally adiabatic boundary with the surroundings.

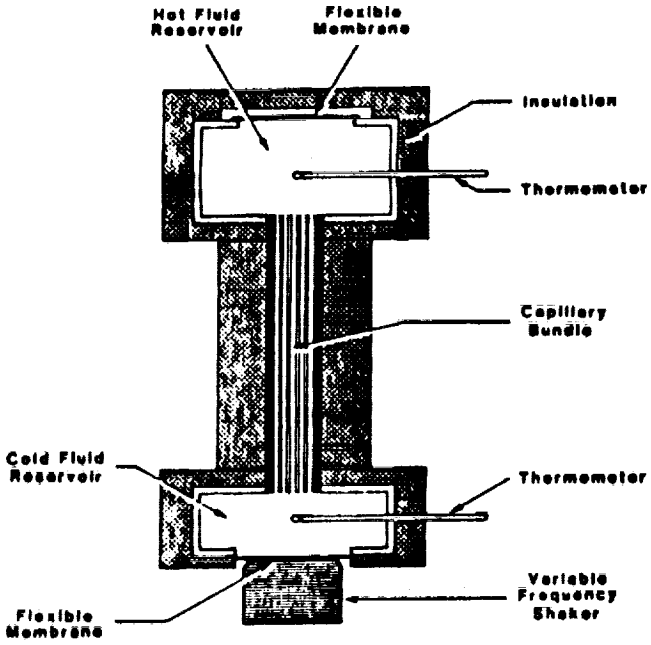


Figure B.1 Kurzweg's test apparatus (reproduced from KZ84)

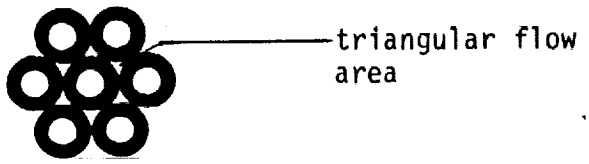


Figure B.2 Typical segment of the tube bundle cross-section

The experimental methodology employed is open to criticism. Initially, the lower (cold) cavity is filled with dyed cold water, while the tube bundle and upper cavity are filled with hot water. Hence, the tidal displacement is determined by measuring the extent of penetration of the dyed water into the tube bundle. It must be noted that such simplicity is prone to errors such as:

- the mass and thermal diffusion of the cold water into the hot water which leads to a "fuzzy" boundary zone making the precise measurement of tidal displacement difficult.

- radial non-uniformity of the flow oscillations arising from the specific geometry of the shaker/flexible membrane interface, that is, the tidal displacements at the center of the tube bundle may be different from those at the containing wall.

- surface tension effects within the capillaries which would complicate the external measurement of the mid-meniscus position.

Kurzweg and Zhao do not appear to acknowledge these problems in the light of the good agreement they obtain (in logarithmic terms) between their analytic and experimental results (KZ84, figure 2). However, since they use a data fitting approach to obtaining this agreement (by adjusting the Prandtl number via the choice of system temperature), it is reasonable to suppose that many of the systematic errors which would degrade this good agreement are buried in the data fitting process.

The upper and lower cavity temperatures are measured via thermometers read at one minute intervals for a total experimental run time of 6 minutes. The heat flowing through the tube and resultant effective diffusivity are determined exclusively from these measurements. In particular, the resulting inferred temporal temperature gradient of the cold cavity (from which the net heat flowing down the tube is computed) is highly approximate in comparison with the instantaneous axial temperature gradient used in the effective diffusivity calculation (KZ84, equation 1) (a time-averaged axial temperature gradient would have been more appropriate). Hence this additional source of systematic error is also embedded in the Prandtl number data fit.

Needless to say, these issues complicate the simulation, particularly when the objective is to obtain agreement with the experimental and "validated" analytic results. However, of perhaps even more importance from a simulation perspective, is the difficulty of simulating the initial discontinuous (literally "brick wall") temperature profile at the tube bundle / cold cavity interface. Such a condition has been documented in the literature (for example, BB75) to magnify the effects of false diffusion in producing erroneous advective fluxes.

Hence within these limitations, the following simulation approach is adopted.

a. All the available physical parameters describing the apparatus and test conditions given in KZ84 are used as described in table B.1.

b. The three additional geometrical parameters needed to implement the simulation were determined by direct measurement of figure B.1 in the hope that the relative scale of the figure is somewhat representative of reality. These parameters are:

Hot/cold cavity cross-sectional area ratio = 1
Stationary hot/cold cavity length ratio = 1.714
Cold cavity / casing cross-sectional area ratio = 4.8

Fortunately, under incompressible flow conditions, errors in these ratios do not effect the flow within the tube bundle provided mass flux boundary conditions are used. They do have an effect when pressure boundary conditions are invoked.

Table B.1 Explicit apparatus and test parameters

| Parameter Description | Parameter Value |
|---|---|
| Number of capillary tubes | 31 |
| Capillary tube length | 200 mm |
| Tube bundle casing diameter | 12.7 mm |
| Capillary tube internal diameter | 1 mm |
| Net flow area | 0.67 $cm^2$ |
| Cold cavity volume | 114 $cm^3$ |
| Cold cavity initial temperature | 22 °C |
| Hot cavity initial temperature | 78 °C |

c. The test point was chosen from KZ84 figure 2 (a logarithmic plot) in terms of Kurzweg's correlation factor $K_K$ which is defined as:

$$K_K = \Delta x^2 \frac{\sqrt{\omega\nu}}{r} \qquad \text{(B.3.1)}$$

where:

$\Delta x$ = tidal displacement
$\nu$ = kinematic viscosity
$\omega$ = angular velocity
$r$ = capillary tube radius

The nominal chosen value of $K_K$ = 122 $cm^2/s$ corresponds to the middle of the test range where evidently three tests were carried out at the same $K_K$ (or three data points from the same test). These three points yield values just above that calculated using the analytic result given by equation (15) in KZ84. Furthermore, at this point in the correlation, the analytic result is bounded below by two additional experimental values at a slightly greater (in a logarithmic context) $K_K$ of 149 $cm^2/s$. Hence the "fit" of the analytic result appears to be very good at this point. The test $K_K$ is achieved by choosing an oscillation frequency of 6 Hz and a tidal displacement of 37.83 mm which both fall within the parameter ranges actually tested.

d. As noted by Kurzweg and Zhao, the accuracy of their analysis is critically dependent upon the choice of temperature at which the fluid parameters are evaluated, particularly the Prandtl number, which is strongly dependent on temperature in the 22 to 78 °C range. Therefore, the fluid parameters used in the simulations are chosen to be those at 60 °C as recommended in KZ84 (figure 2). The relevant parameters for

water at this temperature together with those of glass (necessary for modelling the capillary tube walls) are given in table B.2.

Table B.2 Fluid and wall material properties

| Property | Water (Sc79) | Glass (ASH81) |
|---|---|---|
| Density ($kg/m^3$) | 983.3 | 2470 |
| Specific heat capacity (J/kg.K) | 4191 | 750 |
| Thermal conductivity (W/m.K) | 0.65 | 1.0 |
| Dynamic viscosity (kg/m.s) | $47.0 \times 10^{-5}$ | -- |
| Prandtl number | 3.01 | -- |

It must be pointed out that a better approach would be to include these parameters in the simulation as temperature dependent entities. However, in the interest of reducing the differences between the simulation and the analysis (the major objective being to use the analysis as fitted to the experimental data as the validation standard), it was decided to proceed on the above basis.

e. The method used to calculate the effective diffusivity in the simulation corresponds to that of KZ84 and is given by:

$$\kappa_{eff} = \left(\frac{l}{A}\right)_{tube} \frac{V_c}{(T_h - T_c)} \frac{dT_c}{dt} \qquad (B.3.2)$$

In applying equation (B.3.2), the rate of temperature change in the cold cavity is computed as the net cyclic temperature change rate, that is, the difference between the cold cavity temperatures at the end and beginning of a cycle divided by the period. This enables the change in effective diffusivity to be tracked as a function of time so that the simulation can be terminated as soon as the rate of change of the simulated effective diffusivity becomes small. Ultimately, of course, the effective diffusivity becomes infinite when the hot and cold cavities reach thermal equilibrium. This achieves the same physical purpose as Kurzweg's experimental procedure while minimizing the amount of computation. In practice, a simulation period of .5 minutes proved more than adequate under these conditions.

## B.4 THE FALSE DIFFUSION CORRECTION METHODOLOGY

False diffusion arises in transient continuum mechanics numerical analysis in the discretisation of the advection terms in the conservation balances. Typically, when using any variation of upwind difference or upwind parameter methodology (whether the second upwind difference formulation of

Gentry, Martin and Daly (GM66) or the equilibrium analytic approach of Patankar (Pa80)), the advected flux on the control volume boundary is biased towards the upwind advected parameter rather than the actual value of the parameter at the boundary. In general, the actual value of the advected parameter is different from both the upwind and downwind values in a continuous system. In Stirling machine analysis, false diffusion is known to be a significant cause of error in modelling the working fluid in the regenerator (originally pointed out by Gedeon (Ge84)).

The literature on false diffusion is quite voluminous as it long has been recognized as one of the principal difficulties in numerical analysis. However, most of the algorithms developed for correcting or eliminating false diffusion are based on discretisations of the differential conservation balances, particular examples being the SHASTA algorithm of Book, Boris and Hain (BB75) and the sequential backward difference predictor / forward difference corrector methodology of MacCormack (Mc82). Unfortunately, none of these schemes works well in an integral environment where there are no parameter gradients to be exploited in the advection terms.

The first attempt made was to invoke the upwind linear extrapolation method successfully used in Go87 for modelling false diffusion in the regenerator of Stirling machines. Theoretically, such an approach could be expected to work well in simulating Kurzweg's apparatus, since in time, the temperature profile between the hot and cold cavities becomes linear. However, at startup, in the presence of the discontinuous temperature gradient at the cold cavity entrance, the method fails badly, and later, even under milder temperature gradient conditions, the method yields an over-prediction of the effective diffusivity.

Hence, after much analysis and computation, an apparently effective and unconditionally stable false diffusion correction methodology was developed. The methodology may be described in terms of the following generalized algorithmic sequence:

*a.* Predict the parameter field $\psi^*$ using a conventional second upwind difference spatial discretisation (Go87). In general, an explicit, implicit or hybrid integration scheme may be used for this step.

*b.* Calculate the source term from:

$$K_{source} = \int_{A_n} (\psi^*_{uw} - \psi^*_n)(g_n \cdot n)\, dA \qquad (B.4.1)$$

where:

$\psi^*_{uw} = \psi^*_{i-1}$ if $g_{ni} \geq 0$

$\psi^*_{uw} = \psi^*_i$ if $g_{ni} < 0$

$\psi^*_n = f(\psi^*_i)$

It may be noted that no restrictions need be placed on the form of the interpolating function f provided it is bounded symmetrically, for example, f may be a polynomial of odd order.

*c.* The correction field $\Delta\psi$ is found implicitly from:

$$\frac{M\,\Delta\psi}{\Delta t} = \int_{A_n} \Delta\psi_{uw}(-g_n \cdot -n)\, dA + K_{source} \qquad (B.4.2)$$

where:

$\Delta\psi_{uw} = \Delta\psi_{i-1}$ if $-g_{ni} \geq 0$

$\Delta\psi_{uw} = \Delta\psi_i$ if $-g_{ni} < 0$

*d.* Calculate the corrected parameter field $\psi$ given by:

$$\psi = \psi^* + \Delta\psi \qquad (B.4.3)$$

*e.* Iterate from step *a* until the change in the corrected parameter field $\psi$ becomes appropriately small.

In practice, the iteration required in step *e* does not add to the iterations required in any case to implement the pressure or non-pressure linked algorithms discussed in part A. Two interpolating functions have been tested for use in step *b*, namely linear and cubic polynomials. As shown by the results (section B.7), both schemes produce almost the same results, however, during the transient start-up phase, the cubic function yields a better approximation of the temperature field at the cold cavity entrance.

A negative consequence of the false diffusion correction algorithm described above is that it necessitates one more matrix inversion per conservation equation per iteration. However, in terms of an integral analysis, this is more than offset by at least a six-fold reduction in the required discretisation combined with better accuracy at the coarser discretisation than obtained using the upwind approach alone at the finer discretisation. In this context, it must be pointed out that the flux correction methodology developed is still embryonic and is capable of much enhancement.

## B.5 DEVELOPMENT OF AN ENTROPY TRANSPORT EQUATION

The approach adopted in deriving the entropy transport equation is identical in nature to that documented in Go87 for the mass, momentum and energy balances. The essential difficulty (at least philosophically) is in defining an appropriate entropy postulate. One traditional approach is to define entropy as being that which requires thermodynamic processes to be unidirectional, for example, according to Wark (Wa77):

> "Any system having certain specified constraints and having an upper bound in volume can reach from any initial state a stable equilibrium state with no net effect on the environment."

The corollary to this postulate, known as the Kelvin-Planck statement (Wa77), is sufficient to allow proof of Clausius' inequality as a theorem, that is for a closed system:

$$\oint \frac{\delta Q}{T} \leq 0 \tag{B.5.1}$$

which in turn allows the "increase in entropy" principle to be derived, or:

$$d\Xi \geq \frac{\delta Q}{T} \tag{B.5.2}$$

where $\Xi$ denotes entropy.

Equation (B.5.2) is invoked by some authors directly as an entropic postulational basis, for instance Slattery's entropy postulate (Sl81) that:

> "The minimum rate of production of entropy in a body is proportional to the rate of energy transmission to the body."

or symbolically:

$$\frac{d}{dt}\int_{V_{(m)}} \rho\hat{\Xi}\, dV \geq \int_{A_{(m)}} \left(\frac{\boldsymbol{q}}{T} \cdot -\boldsymbol{n}\right) dA + \int_{V_{(m)}} \frac{\rho\dot{\hat{E}}}{T}\, dV \tag{B.5.3}$$

where the terms on the RHS represent the entropy changes produced by contact energy transmission to the body through its bounding surface and by external and mutual energy transmission respectively.

However, from a computational point of view, neither of these postulates is determinate, that is, they do not allow entropy to be definitely calculated. Hence for this reason, the following entropy postulate based on a statement originally proposed by Truesdell and Toupin (TT60) as the basic assumption of thermodynamics is preferred:

Postulate V A dimensionally independent scalar parameter $\hat{\Xi}$ (termed specific entropy) and the substate densities are sufficient to determine the specific internal energy of a material particle independently of time, place, motion and stress.

That is:

$$\hat{U} = \hat{U}\left(\hat{\Xi}, \rho_i|_{i=1}^{n}, \mathrm{p}\right) \tag{B.5.4}$$

This postulate is not equivalent to those quoted above in the sense that it is not based upon a manifestation of entropy, but rather is an equation of state for internal energy which requires that entropy be a fundamental property. However, the consequences of equation (B.5.4) must satisfy the previous conventional postulates as expressed in a general fashion by equation (B.5.3).

When a particular body is thermodynamically homogeneous, that is every particle p is behaviorally identical, equation (B.5.4) may be simplified to:

$$\hat{U} = \hat{U}\left(\hat{\Xi}, \hat{V}, \Gamma_i\right) \tag{B.5.5}$$

where $\Gamma$ is the mass (or mole) fraction of species $i$. In terms of the single component working fluids being considered here (and hence also for Stirling machines in most cases), it is useful for the sake of simplicity to proceed by considering single specie entities only, that is:

$$\hat{U} = \hat{U}\left(\hat{\Xi}, \hat{V}\right) \tag{B.5.6}$$

Differentiating and noting that $T \equiv \left(\frac{\partial \hat{U}}{\partial \Xi}\right)_{\hat{V}}$ and $P \equiv \left(\frac{\partial \hat{U}}{\partial \hat{V}}\right)_{\hat{\Xi}}$ yields:

$$d\hat{U} = T d\hat{\Xi} - P d\hat{V} \tag{B.5.7}$$

Taking the substantive derivative, multiplying through by $\rho$, substituting Go87 equation (C.7) (which relates the change in size of a discrete volume to the motion of its enclosing boundaries) and simplifying:

$$\rho \frac{D\hat{U}}{Dt} = \rho T \frac{D\hat{\Xi}}{Dt} - P(\nabla \cdot \boldsymbol{v}) \tag{B.5.8}$$

The substantive differential energy balance at every point in a material body is given by (Go87):

$$\rho \frac{D\hat{U}}{Dt} = \rho \dot{\hat{E}} + (\boldsymbol{T} : \nabla \boldsymbol{v}) - P(\nabla \cdot \boldsymbol{v}) - \nabla \cdot \boldsymbol{q} \tag{B.5.9}$$

Equating (B.5.8) and (B.5.9), expanding and rearranging:

$$\rho \frac{D\hat{\Xi}}{Dt} = \frac{\rho \dot{\hat{E}}}{T} + \frac{(\boldsymbol{T}:\nabla \boldsymbol{v})}{T} - \nabla \cdot \frac{\boldsymbol{q}}{T} - \frac{\boldsymbol{q}}{T^2} \nabla T \tag{B.5.10}$$

Integrating (B.5.10) over the material body volume $V_{(m)}$ and substituting Go87 equations (C.9) and (C.10) yields after simplification and rearrangement:

$$\frac{d}{dt} \int_{V_{(m)}} \rho \hat{\Xi} \, dV = \int_{V_{(m)}} \left\{ \frac{\rho \dot{\hat{E}}}{T} + \frac{(\boldsymbol{T}:\nabla \boldsymbol{v})}{T} - \frac{\boldsymbol{q}}{T^2} \nabla T \right\} dV + \int_{A_{(m)}} \left( \frac{\boldsymbol{q}}{T} \cdot -\boldsymbol{n} \right) dA \tag{B.5.11}$$

Rearranging the right hand side:

$$\frac{d}{dt} \int_{V_{(m)}} \rho \hat{\Xi} \, dV = \int_{A_{(m)}} \left( \frac{\boldsymbol{q}}{T} \cdot -\boldsymbol{n} \right) dA + \int_{V_{(m)}} \frac{\rho \dot{\hat{E}}}{T} \, dV + \int_{V_{(m)}} \left\{ \frac{(\boldsymbol{T}:\nabla \boldsymbol{v})}{T} - \frac{\boldsymbol{q}}{T^2} \nabla T \right\} dV \tag{B.5.12}$$

Comparing equations (B.5.12) and (B.5.3) and noting that the last integral on the RHS of (B.5.12) is strictly positive (because $\boldsymbol{q} = -k \nabla T$ ), reveals that the postulational basis of equation (B.5.4) indeed satisfies the conventional entropy postulate as defined by equation (B.5.3) while simultaneously being determinate.

Converting equation (B.5.10) into partial temporal derivative form and substituting into the generalized transport equation (Go87, equation (C.12)) yields the final version of the entropy balance:

$$\begin{aligned} \frac{d_{[V]} \bar{\hat{\Xi}} M}{dt} = & \int_{V_{(s)}} \frac{1}{T} \left\{ \rho \dot{\hat{E}} + (\boldsymbol{T}:\nabla \boldsymbol{v}) - \frac{\boldsymbol{q}}{T} \nabla T \right\} dV + \int_{A_{(s)}} \left( \frac{\boldsymbol{q}}{T} \cdot -\boldsymbol{n} \right) dA \\ & + \int_{A_{(s)}} \rho \hat{\Xi} \left\{ (\boldsymbol{v} - \boldsymbol{v}_{(s)}) \cdot -\boldsymbol{n} \right\} dA \end{aligned} \tag{B.5.13}$$

In implementing the entropy transport equation, it was found that great care must be taken in locating the entropy boundary (within which the cyclic entropy is computed) and in describing the thermal transport across that boundary. In this context, it should be noted that, by definition, the second law of thermodynamics treats isolated systems so that Clausius' inequality applies over the integral of the subsystems of which the isolated system is comprised. In the limit, the only true isolated system is the entire universe, so that extracting a computationally isolated system which can in general exchange heat with its superordinate body is not obvious in all cases.

The approach adopted may be visualized in terms of figure B.3.

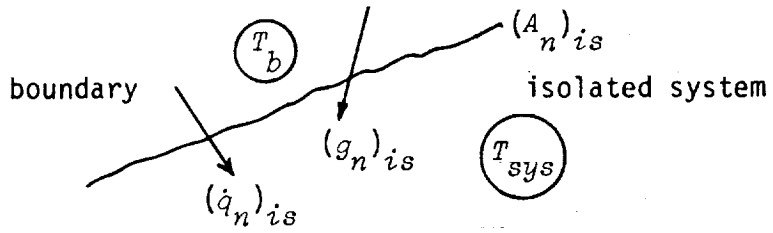


Figure B.3 Isolating boundary entropy contribution

Consider a segment of the isolating boundary $(A_n)_{is}$ across which flows a mass flux $(g_n)_{is}$ and a thermal diffusion flux $(\dot{q}_n)_{is}$ . The operating entropic principle governing the isolating boundary is:

> The net contribution of the entropic and thermal fluxes crossing the isolating boundary is assigned to the isolated system entropy irrespective of the spatial location of these fluxes (which in general span a part of the isolated system as well as the bounding environment).

Hence, applying equation (B.5.13) to the situation depicted in figure B.3 yields:

$$\frac{d_{[V]}\bar{\Xi}M}{dt} = \left[\frac{d_{[V]}\bar{\Xi}M}{dt}\right]_{internal} + \int_{(\alpha V)_b} \frac{-\{(\dot{q}_n)_{is}\nabla T_b\}}{T_b^2}\,dV + \int_{(\alpha V)_{sys}} \frac{-\{(\dot{q}_n)_{is}\nabla T_{sys}\}}{T_{sys}^2}\,dV + \int_{(A_n)_{is}} \left[\frac{(\dot{q}_n)_{is}}{T_{sys}-T_b}\cdot -n\right] dA \qquad \text{(B.5.14)}$$

where $\alpha$ is an appropriate fraction for delineating the integration sub-volume (typically $\alpha = .5$ for a conformal Cartesian mesh). It should be noted that the advection entropy flux does not appear in equation (B.5.14) because its net contribution to the isolated system entropy is zero.

The success in using the full entropy transport equation including generalized isolated boundary heat transport may be judged from the results presented in section B.7. As envisaged when proposing this study, Kurzweg's laminar flow apparatus provides an ideal test bed for such an entropy transport equation, since the transport of entropy is clearly visible from a system perspective and not compartmentalized between system components as occurs, for example, in Stirling machines.

## B.6 OTHER ISSUES

During the process of testing the false diffusion correction algorithm, it was found that careful attention had to be paid to modelling the conduction heat transfer in the capillary tube walls. In particular, the effective

diffusivity was found to be sensitive to the manner in which the wall/fluid interface is discretised, both in the capillary tubes as well as in the hot and cold cavities. Although in the simulations (both one- and two-dimensional) the capillary tube walls are modelled as axially discretised, one-dimensional entities and this approach seems to yield good results, there is a suspicion that a one-dimensional approach is probably inadequate, particularly at high radial heat transfer rates. Thus, in the future, thought should be given to modelling Stirling heat exchanger walls as radially discretised two-dimensional entities to determine whether the above suspicion has any basis.

Finally, as the results show, the limitations of a first order temporal integration scheme became manifest, particularly in the two-dimensional simulation. However, owing to time constraints, the first order temporal integration algorithm in the METR two-dimensional code could not be upgraded to second order (a second order one-dimensional code had been developed and tested previously (Go90)).

## B.7 RESULTS

The results of all the simulations undertaken are summarized in table B.3. At the chosen test point, the effective diffusivity produced by Kurzweg's analysis amounts to 4.8 $cm^2/s$ with the corresponding experimental values ranging between 5.8 and 7.4 $cm^2/s$. Using an axial discretisation of 30 discrete volumes (.15 discrete volumes per millimeter) and a temporal discretisation of 100 increments per cycle, the first order one-dimensional simulation with no false diffusion correction over-predicted the effective diffusivity by a range of 2.9 to 4.4 times (corresponding to the upper experimental and analytic values respectively). As noted above, including the false diffusion correction produced a simulated value for effective diffusivity within the experimental range and at most 36% greater than that analytically predicted. In contrast, upgrading the one-dimensional simulation to second order temporal accuracy, reduced the over-prediction of effective diffusivity with no correction to a range of 2.6 to 4.1 times. Including either linear or cubic false diffusion correction produced a result within 3.5% of the analytic value.

Applying the second-order simulation at two other values of $K_K$ using cubic false diffusion correction yields the results compiled in table B.4.

As discussed in section B.3 above, in view of the experimental uncertainties, perhaps the "fitted" analytic value is indeed a reasonable estimate of the actual effective diffusivity, in which case, discrepancies less than 3.5% are an adequate validation of the false diffusion correction methodology.

Table B.3 Simulation results

| Data Source | False Diffusion Correction Method | Axial Discretisation (increments) | Radial Discretisation (increments) | Temporal Discretisation (incs/cycle) | Heat Transfer Coefficient Multiplier | Effective Diffusivity ($cm^2/s$) |
|---|---|---|---|---|---|---|
| Kurweg's analysis | -- | -- | -- | -- | -- | 4.8 |
| Experimental measurement | -- | -- | -- | -- | -- | 5.8 - 7.4 |
| 1-dimensional simulation: first order temp. integ. | none | 30 | -- | 100 | 1 | 21.2989 |
| | linear | 30 | -- | 100 | 1 | 6.4649 |
| | cubic | 30 | -- | 100 | 1 | 6.5139 |
| 1-dimensional simulation: second order temp. integ. | none | 30 | -- | 100 | 1 | 19.4351 |
| | linear | 30 | -- | 100 | 1 | 4.9545 |
| | cubic | 30 | -- | 100 | 1 | 4.9459 |
| 2-dimensional simulation: - first order temp. integ. | none | 30 | 8 | 400 | -- | 31.3910[1] |
| | linear | 30 | 8 | 400 | -- | 5.7301 |
| - flux boundary condition | linear | 30 | 8 | 600 | -- | 5.1107 |
| 2-dimensional simulation: - first order temp. integ. | none | 30 | 8 | 400 | -- | 31.5080[1] |
| - pres. boundary condition | linear | 30 | 8 | 400 | -- | 5.9171 |

Note

1. Unconverged - for qualitative comparison only.

Table B.4 Effective diffusivity comparison

| Correlation Factor $K_K$ ($cm^2/s$) | Effective Diffusivity ($cm^2/s$) | | | Analysis/ Simulation Discrepancy (%) |
|---|---|---|---|---|
| | Kurzweg's Analysis | Experimental | 1-d Simulation (cubic correction) | |
| 122.0 | 4.8 | 5.8 - 7.4 | 4.9459 | 3.04 |
| 286.1 | 11.31 | 11.1 | 11.0539 | 2.26 |
| 818.5 | 32.36 | 19.1 - 25.9 | 31.2692 | 3.37 |

However, of perhaps more interest, is the observation that all the one-dimensional simulations were carried out using the nominal steady-state Kays and London correlations without the necessity of any heat transfer coefficient multipliers. For all these simulations, the Valensi number (square of the Womersley number) is 19.7 which remains constant because it is independent of tidal displacement. $K_K$ was varied in the simulations via the tidal displacement while the frequency was kept constant at 6 Hz.

At a Valensi number of about 20, Uchida's analysis (Uc56) of oscillating laminar flows as quoted by Simon and Seume (SS86), yields amplitude coefficients of pressure drop and wall shear stress of about 3.1 and 1.3 respectively. Also, at this Valensi number, Uchida's analysis predicts lead phase angles of pressure drop and wall shear stress of approximately 68° and 28° respectively. Noting that for steady flow the amplitude coefficients are unity and the lead phase angles are zero, it is evident that the simulations represent a flow regime which is different from steady flow (particularly in phase lead terms). Hence in view of the good agreement obtained in table B.4, an argument can be made for the adequacy of the steady-state correlations for predicting heat transfer under laminar oscillating flow conditions at Valensi numbers less than 20 when the effects of false diffusion are minimized (if not eliminated).

In developing the two-dimensional results, the importance of temporal discretisation has already been alluded to. For this, reason, the high temporal discretisations required to minimize the limitations of the first order temporal integration algorithm used placed a severe load on the available computing resources which constrained the number of runs carried out to the half-minute closure point.

The axial discretisation was maintained at 30 discrete volumes while the radial discretisation could be comfortably limited to 8 discrete volumes. With the false diffusion correction activated, increasing either of these values produced a negligible change in the end result.

Hence in this context, other than the temporal discretisation, the only significant parameter was found to be the mass flux boundary condition. Two conditions were tested, namely:

- specifying a radially uniform flow at the cold end tube entrance equal to the rate of change of the cold cavity volume.

- using the rate of cold cavity volume change to generate a sinusoidally varying pressure which in turn allows the entrance mass fluxes to be calculated (a somewhat nebulous approach in the light of the paucity of data describing the hot and cold cavities).

In both cases, the hot cavity is treated as being isobaric at atmospheric pressure and gravity induced buoyancy forces are included in the momentum balance.

In all cases, the uniform flux boundary condition produced slightly better results as might be expected. A shown in table B.3, only the linear false diffusion correction methodology was tested. At a temporal discretisation of 400 increments per cycle, the uniform flow boundary condition simulation produced an effective diffusivity between the experimental and analytic values, while increasing the discretisation to 600 increments per cycle yields a simulated diffusivity 6.5% higher than the analytic result and shows the diffusivity converging to the value predicted using the second order one-dimensional code. Nevertheless, while yielding a satisfactory result, a discretisation of 600 increments per cycle is not practical for an implicit code.

At the half minute cut-off, the false diffusion correction was deactivated with a resultant escalation of the effective diffusivity to an unconverged value in excess of 30 $cm^2/s$. This is indicative qualitatively of the effectiveness of the false diffusion correction algorithm in two dimensions.

The results produced by the entropy transport equation are depicted in figures B.4 through B.9. Figure B.4 shows that the entropy is highest midway along the tube bundle and decreases towards both cavities. The hot cavity always has a lower entropy than the cold cavity. Numerical output from the simulation (not shown) confirms that the cyclic integral of the entropy over the entire fluid system increases monotonically.

The cyclic temperature surface is depicted in figure B.5. Essentially, this shows a fairly invariant linear temperature profile flattening alternately in the regions adjacent to the hot and cold cavities as the mass flux reverses direction.

Combining figures B.4 and B.5 yields the temperature-specific entropy ($T$-$\Xi$) diagrams of figures B.6 to B.9. Within the tube, figures B.7 and B.8 show closed cycles whose areas are exactly equal to the generated cyclic irreversibilities at those locations. As the tube acts as a thermal transfer device between the hot and cold cavities and is externally adiabatic, closure of the $T$-$\Xi$ diagrams is thermodynamically necessary and thus an indication that

the entropy transport equation is operating correctly. All the entropy generated in the tube is pumped towards the hot and cold cavities, both of whose entropies must increase monotonically which indeed is the case as shown in figures B.6 and B.9. In figure B.6, during the first part of the cycle when the flow is positive (that is, from the cold to the hot cavity), the specific entropy increases marginally while the temperature drops (dissipation is not explicitly included in the cavities because of the absence of adequate geometrical data, see section B.3). When the flow reverses, the entropy generated in the capillary tubes is transported into the cold cavity so producing the requisite monotonic cyclic entropy increase.

The inverse process occurs in the hot cavity as shown in figure B.9. During the first half of the cycle when the flow is positive, entropy is transported into the hot space while its temperature decreases. Notice that over the cycle, the hot space has cooled while the cold space has become warmer.

At first sight, it may seem unreasonable that the temperature of the cold cavity decreases during positive flow and the hot cavity temperature increases during negative flow. However, bearing in mind that in an integral analysis the reported temperatures are the volume-averaged temperatures and that an axial temperature gradient exists through the cavities, then as mass is removed from a cavity, its volume-averaged temperature must change. Hence, in the cold cavity, the removed fluid is hotter than the remaining fluid and hence the volume-averaged temperature decreases, with the inverse process occurring in the hot cavity. This is a direct consequence of the flux correction methodology and reveals how it provides a more accurate description of the continuum mechanics than the upwind difference approach. In particular, in the absence of diffusion heat transfer from the ends of the capillary tubes, the upwind algorithm yields constant temperatures in the cavities during their respective periods of mass efflux.

# Figure B.4 ENTROPY SURFACE
## Kurzweg's Oscillating Flow Apparatus
### 1–Dimensional Simulation

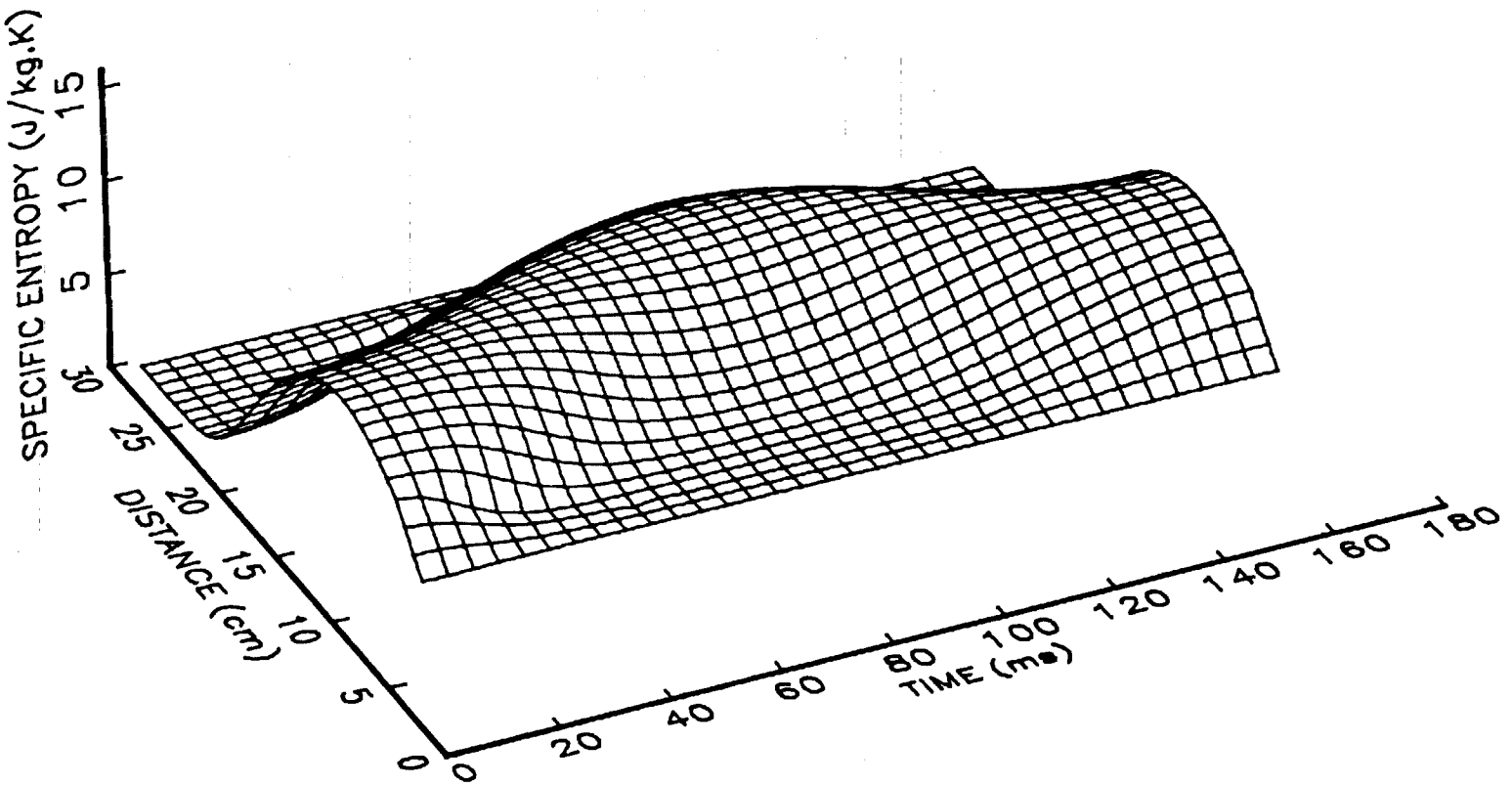


Note: Distance measured from cold end

Figure B.5 TEMPERATURE SURFACE
Kurzweg's Oscillating Flow Apparatus
1–Dimensional Simulation

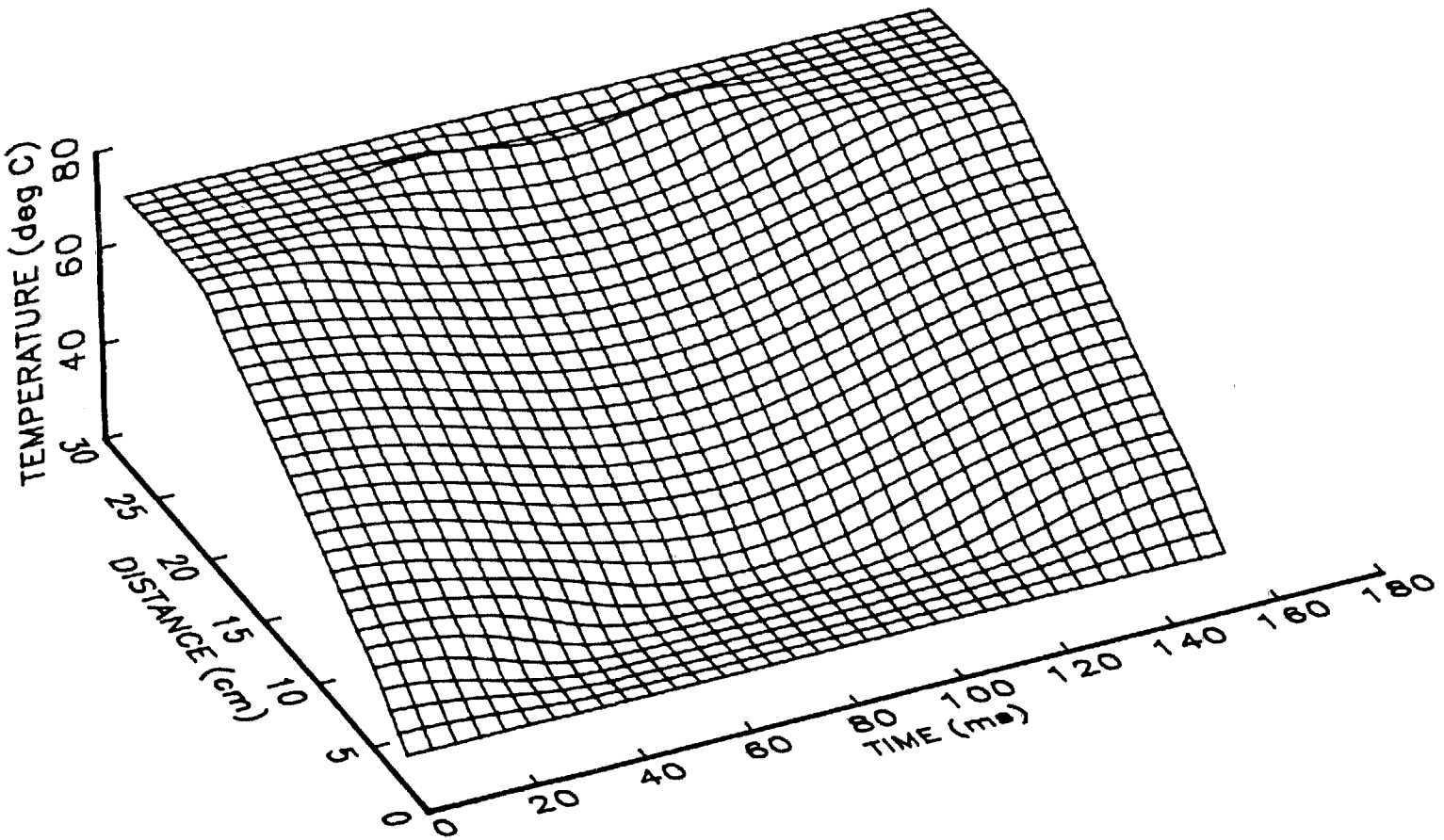


Note: Distance measured from cold end

Figure B.6 COLD CAVITY IRREVERSIBILITY PROFILE

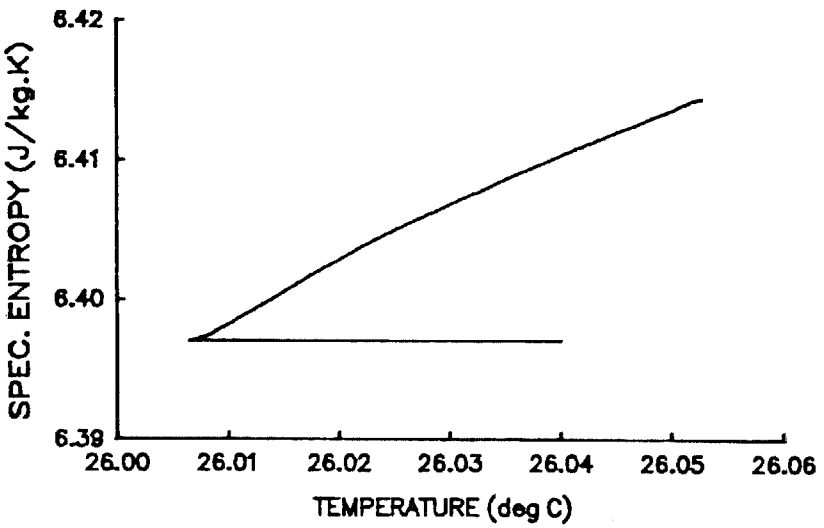


Figure B.7 TUBE IRREVERSIBILITY PROFILE
Cold Cavity End

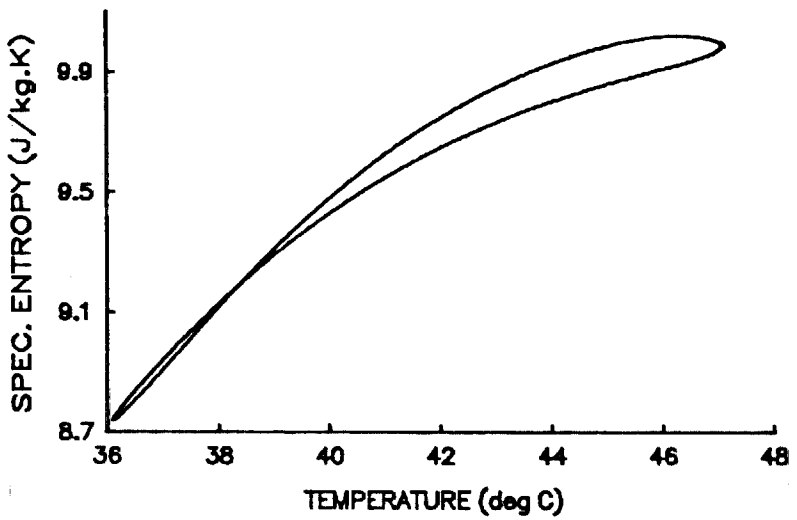


Figure B.8 TUBE IRREVERSIBILITY PROFILE
Hot Cavity End

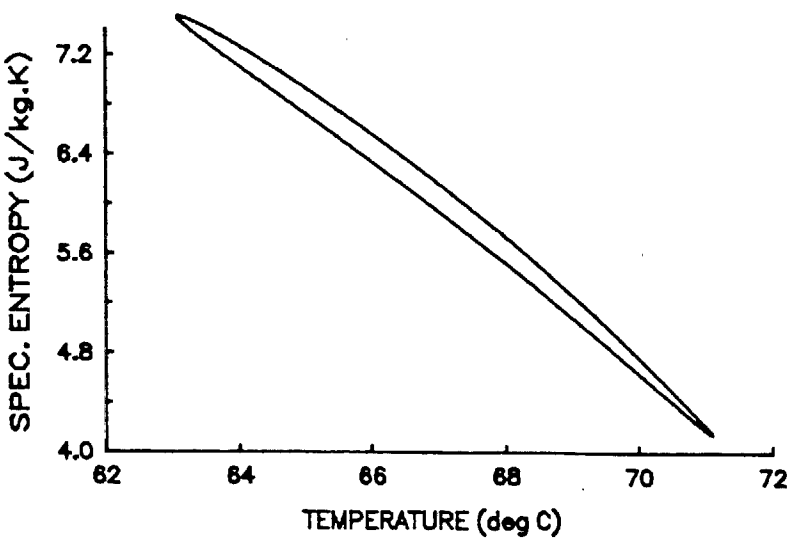


Figure B.9 HOT CAVITY IRREVERSIBILITY PROFILE

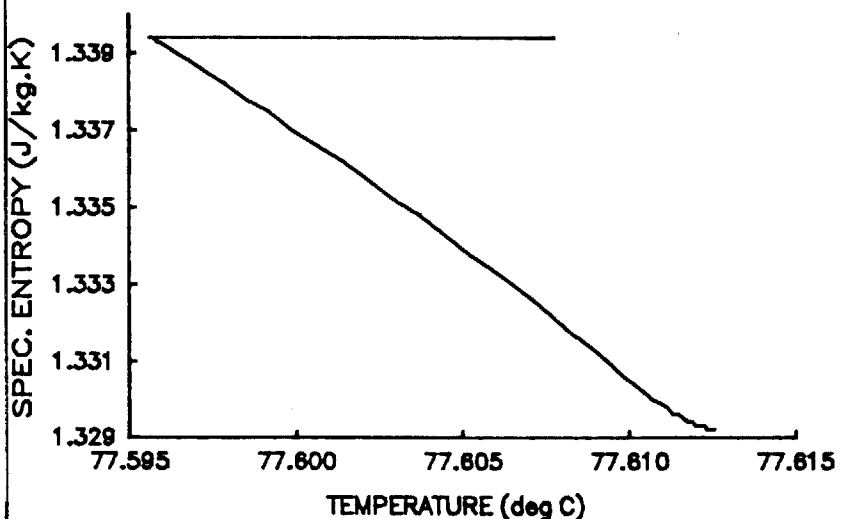

## B.8 CONCLUSION

The significant results obtained from the work carried out in part B, have been the development of a tentatively effective false diffusion correction methodology, its demonstration in one- and two-dimensional simulations and the development and evaluation of a rigorous entropy transport equation. Using Kurzweg's oscillating flow apparatus as the target hardware, in terms of the prevailing geometrical and experimental uncertainties, the simulated data compare favorably with those generated analytically and experimentally.

A comparison of the simulation and experimental/analytic data suggests that under laminar, incompressible flow conditions at Valensi numbers less than 20, standard steady-state heat transfer correlations are adequate for predicting oscillating flow boundary heat transfers provided that the effects of false diffusion are accounted for in the simulation.

Use of a full entropy transport equation in the simulation provides useful physical insights into the irreversibility processes occurring within oscillating flows.

The results produced should shed some additional light on the loss mechanisms occurring within Stirling cycle machines, at least in terms of isolating possible sources of error in existing simulation design codes.

## C L O S U R E

The work carried out in part A suggests that the next logical steps for investigating information propagation effects in Stirling machines might be:

- the development and validation of a simulation based on a solution of the full second order wave equation or Kirchoff momentum equation.

- a transmission line based investigation and validation of MacCormack's characteristic factorization algorithm.

- an experimental program to measure information propagation effects in transmission lines and Stirling machines using precise digital acoustic techniques. These tests should emphasize the accurate measurement of phase angles in order to validate this aspect of Iberall's analysis as well as to determine the information propagation characteristics of actual Stirling hardware.

The results of part B suggest that the false diffusion correction methodology developed may yield some improvement in the accuracy of existing one-dimensional Stirling machine simulation codes. This improvement would result from standard steady-state heat transfer correlations yielding better accuracy while the enthalpy fluxes at the heater and cooler entrance and exit ports also would be more accurately modelled.

Inclusion of entropy transport (as opposed to entropy generation alone) in Stirling machine codes would yield a reliable method for tracking irreversibilities within the engine and would allow a better comparison of the performance of different simulation codes. Hence, as a next step, it seems appropriate that the false diffusion correction algorithm and entropy transport equation be ported to existing codes which should then be re-validated against experimental data.

## REFERENCES


ASH81 American Society of Heating, Refrigeration and Air-Conditioning Engineers. *Handbook of 1981 Fundamentals*, ASHRAE, Atlanta, 1981.

BB75 Book, D.L., Boris, J.P. and Hain, K. 'Flux-Corrected Transport II: Generalizations of the Method', *Journal of Computational Physics*, vol. 18, 1975, pp. 248-283.

Ge84 Gedeon, D. 'Numerical Advection Errors in Stirling Cycle Nodal Analyses', *Proceedings of the 19th IECEC*, paper no. 849101, San Francisco, 1984.

GM66 Gentry, R.A., Martin, R.E. and Daly, B.J. 'An Eulerian Differencing Method for Unsteady Compressible Flow Problems', *Journal of Computational Physics*, vol. 1, 1966, pp. 87-118.

Go68 Goldschmeid, F.R. *On the Dynamic Performance of Viscous Compressible Fluids in Rigid Tubes with Volume Termination as a Function of Stokes Number*, NASA TM X-53785, 1968.

Go87 Goldberg, L.F. *A State Space and Continuum Mechanics Analysis of Stirling Cycle Machines*, PhD Thesis, University of the Witwatersrand, Johannesburg, 1987.

Go90 Goldberg, L.F. *One- and Two-Dimensional Stirling Machine Simulation Using Experimentally Generated Reversing Flow Turbulence Models*, NASA contractor report no. 185285, 1990.

Ib50 Iberall, A.S. *Attenuation of Oscillatory Pressures in Instrument Lines*, research paper RP2115, vol. 45, NBS, 1950.

Ji73 Jimenez, J. "Nonlinear gas oscillations in pipes. Part I. Theory", *Journal of Fluid Mechanics*, vol. 59, part 1, 1973, pp. 23-46.

KL64 Kays, W.M. and London, A.L. *Compact Heat Exchangers*, 2nd edition, McGraw-Hill, New York, 1964.

Ko90 Kohler, W.J. *Numerical Prediction of Turbulent Oscillating Flow and Associated Heat Transfer*, PhD Thesis, University of Minnesota, Minneapolis, 1990.

KZ84 Kurzweg, U.H. and de Zhao, L. 'Heat transfer by high-frequency oscillations: A new hydrodynamic technique for achieving large effective thermal conductivities', *Phys. Fluids*, vol. 27, no. 11, 1984, pp. 2624-2627.

Mc82 MacCormack, R.W. "A Numerical Method for Solving the Equations of Compressible Viscous Flow", *AIAA Journal*, vol. 20, no. 9, 1982, pp. 1275-1281.

OJ89 Organ, A.J. and Jung, P.S. "The Stirling cycle as a linear wave phenomenon", *Proceedings IMechE*, vol. 203, 1989, pp 301-309.

Or82 Organ, A.J. "Gas Dynamics of the temperature determined Stirling cycle", *Journal of Mechanical Engineering Science*, vol. 23, no. 4, 1982, pp. 207-216.

Pa80 Patankar, S.V. *Numerical Heat Transfer and Fluid Flow*, Hemisphere, Washington D.C., 1980.

Ro82 Roache, P.J. *Computational Fluid Mechanics*, Hermosa Publishers, Albuquerque, 1982.

St45 Strutt, J.W. (Lord Rayleigh) *The Theory of Sound* (Vol. II), 2nd edition, Dover, New York, 1945.

Sc79 Schlichting, H. *Boundary-Layer Theory*, 7th edition, McGraw-Hill, New York, 1979.

SS86 Seume, J. and Simon, T. 'Oscillating Flow in Stirling Engine Heat Exchangers', *Proceedings of the 21st IECEC*, paper no. 869118, San Diego, 1986.

TT60 Truesdell, C. and Toupin, R.A. In *Handbuch der Physik*, Flugge, S. (editor), vol. 3/1, Springer-Verlag, Berlin, 1960.

Wa65 Watts, G.P. *An Experimental Verification of a Computer Program for the Calculation of Oscillatory Pressure Attenuation in Pneumatic Transmission Lines*, report no. LA-3199-MS, Los Alamos Scientific Laboratory, 1965.

Wa77 Wark, K. *Thermodynamics*, 3rd. edition, McGraw-Hill, New York, 1977.

# REPORT DOCUMENTATION PAGE

Form Approved
OMB No. 0704-0188



| 1. AGENCY USE ONLY (*Leave blank*) | 2. REPORT DATE | 3. REPORT TYPE AND DATES COVERED |
|---|---|---|
| | April 1992 | Final Contractor Report |

**4. TITLE AND SUBTITLE**

An Investigation of the Information Propagation and Entropy Transport Aspects of Stirling Machine Numerical Simulation

**5. FUNDING NUMBERS**

WU-590-13-11
C-C-22742-P

**6. AUTHOR(S)**

Louis F. Goldberg

**7. PERFORMING ORGANIZATION NAME(S) AND ADDRESS(ES)**

University of Minnesota
790 Civil and Mineral Engineering Bldg.
Minneapolis, Minnesota 55455

**8. PERFORMING ORGANIZATION REPORT NUMBER**

None

**9. SPONSORING/MONITORING AGENCY NAMES(S) AND ADDRESS(ES)**

National Aeronautics and Space Administration
Lewis Research Center
Cleveland, Ohio 44135-3191

**10. SPONSORING/MONITORING AGENCY REPORT NUMBER**

NASA CR-189143

**11. SUPPLEMENTARY NOTES**

Project Manager, Roy C. Tew, Power Technology Division, NASA Lewis Research Center, (216) 433-8471.

**12a. DISTRIBUTION/AVAILABILITY STATEMENT**

Unclassified - Unlimited
Subject Category 34

**12b. DISTRIBUTION CODE**

**13. ABSTRACT** (*Maximum 200 words*)

Aspects of the information propagation modelling behavior of integral Stirling machine computer simulation programs are investigated in terms of a transmission line. In particular, the effects of pressure-linking and temporal integration algorithms on the amplitude ratio and phase angle predictions are compared against experimental and closed-form analytic data. It is concluded that the discretised, first order conservation balances may not be adequate for modelling information propagation effects at characteristic numbers less than about 24. An entropy transport equation suitable for generalized use in Stirling machine simulation is developed. The equation is evaluated by including it in a simulation of an incompressible oscillating flow apparatus designed to demonstrate the effect of flow oscillations on the enhancement of thermal diffusion. Numerical false diffusion is found to be a major factor inhibiting validation of the simulation predictions with experimental and closed-form analytic data. A generalized false diffusion correction algorithm is developed which allows the numerical results to match their analytic counterparts. Under these conditions, the simulation yields entropy predictions which satisfy Clausius' inequality.

| 14. SUBJECT TERMS | 15. NUMBER OF PAGES |
|---|---|
| Stirling engine; Oscillating flow; Numerical simulation | 52 |
| | 16. PRICE CODE: A04 |

| 17. SECURITY CLASSIFICATION OF REPORT | 18. SECURITY CLASSIFICATION OF THIS PAGE | 19. SECURITY CLASSIFICATION OF ABSTRACT | 20. LIMITATION OF ABSTRACT |
|---|---|---|---|
| Unclassified | Unclassified | Unclassified | |

NSN 7540-01-280-5500

U.S. GOVERNMENT PRINTING OFFICE: 1992 - 648-034/40067

Standard Form 298 (Rev. 2-89)
Prescribed by ANSI Std. Z39-18
298-102